LUND UNIVERSITY

An Atom Probe Investigation of the Effect of Nitrogen in Hot Work Tool Steel

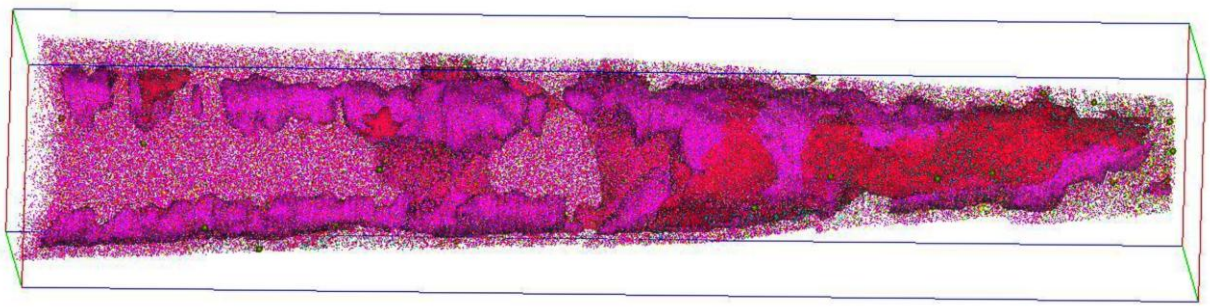

Muhammad Arbab Rehan

Thesis for the Degree of Masters of Science in Physics.

An Atom Probe Investigation of the Effect of Nitrogen in Hot Work Tool Steel

Muhammad Arbab Rehan

Master's Thesis Report (March 2012)
Lund University, Lund, Sweden.

Preface

This thesis project is part of a Master's Degree Program in Physics, Lund University, Sweden. It was carried out in Department of Applied physics (Division of Microscopy and Microanalysis), Chalmers University of Technology, Gothenburg, Sweden.

The work was carried out from September 2011 to March 2012.

The project was supported by Uddeholms AB. They also provided the test materials. Some of the useful information about the test material was taken from the previous work done on similar kind of material from Dr. Jörgen Anderrson, Department of Materials Technology, Uddeholm AB, Sweden.

The project was carried under the supervision of Dr. Mattias Thuvander.

Abstract

Two different hot work tool steels, QRO 90 and QRO 80N were investigated using atom probe tomography. QRO 90 is a commercial alloy while QRO 80N is an experimental test alloy. The main composition of QRO 90 is 0.38C-2.6Cr-2.3Mo-0.9V-0.75Mn (wt%) whereas QRO 80N has the composition 0.38C-1.7Cr-2.7Mo-1.2V-1.1Mn-0.044N (wt%). Hence the main difference between both materials is the nitrogen addition, but there is also an increase in the concentrations of Mo, V and Mn, and a decrease in Cr in QRO 80N. The alloys were investigated after tempering for 1h and 30h, respectively. Previous work has shown an increased tempering resistance of QRO 80N.

Atom probe analysis showed that QRO 80N and QRO 90 have MC type carbides with a mixed composition of Mo and V. The number density of the carbides decreases with tempering suggesting that the small precipitates dissolves during the tempering providing more V and Mo to big carbides. Mo, V and C are strongly depleted in the matrix due to carbide precipitation. After 30 hours of tempering the carbides in both materials are still MC type. However, they become more V-rich, at the expense of Mo. The Mo/V ratio in the carbides changes from 1.4 to 1.1 in QRO 80N while it changes from 2.2 to 1.0 in QRO 90. The only difference between the materials is that the carbides in QRO 90 have a homogenous distribution of V and Mo; in contrast QRO 80N has an inhomogeneous distribution of Mo and V in the carbides. It is also seen that N is strongly enriched in the V-rich areas inside the carbides. However, the average N content of the carbides is only slightly higher in QRO 80N than in QRO 90.

The difference between the secondary carbides in the two steels is not very large and thus it is difficult to determine the reason for the improved tempering resistance. The separation into V-rich (and N-rich) and Mo-rich regions of the carbide could be due to the addition of nitrogen in the QRO 80 N or it could be a consequence of the increase in V and Mo and the decrease in Cr.

Further investigations on materials tempered for different periods of time can provide a good insight about the material. It could be beneficial in understanding the evolution from early stage precipitation to thermally stable carbides.

TABLE OF CONTENT

1. Introduction

Steel is a mixture of Iron and Carbon with usually some amounts of alloying elements. Due to its good hardness and tempering resistance, it is used as tools in industries to form and cast other material e.g ceramics, metals and plastics. Almost all commercial products have somehow been touched by tool steels during their industrial manufacturing. Some of the important tools are forging dies, cutting tools, extrusion dies and industrial knives etc.

Tool steel is categorized on the basis of constructional methodology as oil hardening steel, air hardening steel and water hardening steel or on its working environment as high speed steel, cold work steel and hot work steel. In general, different methods and chemical composition like carbon and alloying elements are used in different proportion to produce the required tool steels.

Hot work tool steel are used at high temperatures. The good tempering resistance is achieved with an average of less than 15 at % alloying content, less than 5 at % Cr and less than 4 at % of Mo, V and W [1].

QRO 90 is a Cr-V-Mo alloyed martensitic hot work tool steel. It is mostly used in high temperature environment ($200^{o}C$ - $600^{o}C$) where there is a need for high thermal fatigue and high tempering resistance for e.g. die casting, forging and extrusion [2]. Elevated temperatures affect the lifetime of tools. In order to achieve a longer lifetime and a better tempering resistance QRO type steels have been modified from time to time.

Uddeholm AB has developed a low chromium hot work tool steel known as 'UDDEHOLM QRO 90 Supreme'. The lowered Cr content (1.5-2.0 wt%) has revealed better hot-hardenability and heat conductivity [3]. The presence of thermally stable precipitates (equilibrium carbides) are the reason behind the better tearing resistance and the good hardenability of hot work tool steel. Lowering chromium comes out to be a good choice for hot work tool steel.

QRO 80N is a test alloy made by addition of small amount of nitrogen to QRO 80. It has also some difference of concentration of alloying elements as compared to QRO 90. It is believed that C+N steel has lower initial hardness but during tempering it achieves a higher hardness than the carbon containing steel [4].

Atom probe Tomography (APT) is a powerful technique used to study nano-sized precipitate at atomic level. It gives detail of atoms present at interfaces, grain boundaries, and in precipitates or in matrix. The results are fruitful to understand the thermodynamical evolution of precipitates. With the help of a high electrical field ions are evaporated from the surface of the material to produce a tomographic image using a position sensitive time of flight detector.

1.1 Background

The martensite has a lath like microstructure with bundles having the same crystallographic orientation. The lath martensite has a high dislocation density and has low angle boundaries between the laths.

Furthermore, the precipitates found in QRO 90 tempered twice at 625°C for 2 hours have M_2C and M_3C type carbides. The sample was analyzed using bright field image of TEM while the dark field image of TEM shows traces of MC carbides. M_2C carbides have rod or plate/disc type structure while MC carbides are smaller in size and spherical in shape [1]. The properties of these carbides are shown in table 1.

The microstructural evolution of carbides in QRO 90 follows the following sequence of carbide transformation [5]:

1. $M_3C \rightarrow M_2C + MC$
2. $M_2C \rightarrow M_6C + MC$

Where as the equilibrium phases of carbides are M_6C, $M_{23}C_6$ and MC [5].

Also, the addition of small quantity of nitrogen in QRO 80N has positive effect on its tempering resistance [1]. The hardness curve for the material is shown in the fig.1.

Table 1 Dimensions and shape of secondary carbides [1].

Type of precipitation	*Diameter (nm), Length (nm), shape*
MC	2-3, spherical
M_2C	D= 2-5, L= 20, rod; D= 20, L =2-5, plate/disc
M_3C	D=30-40, oval; D =30, L=110, rod

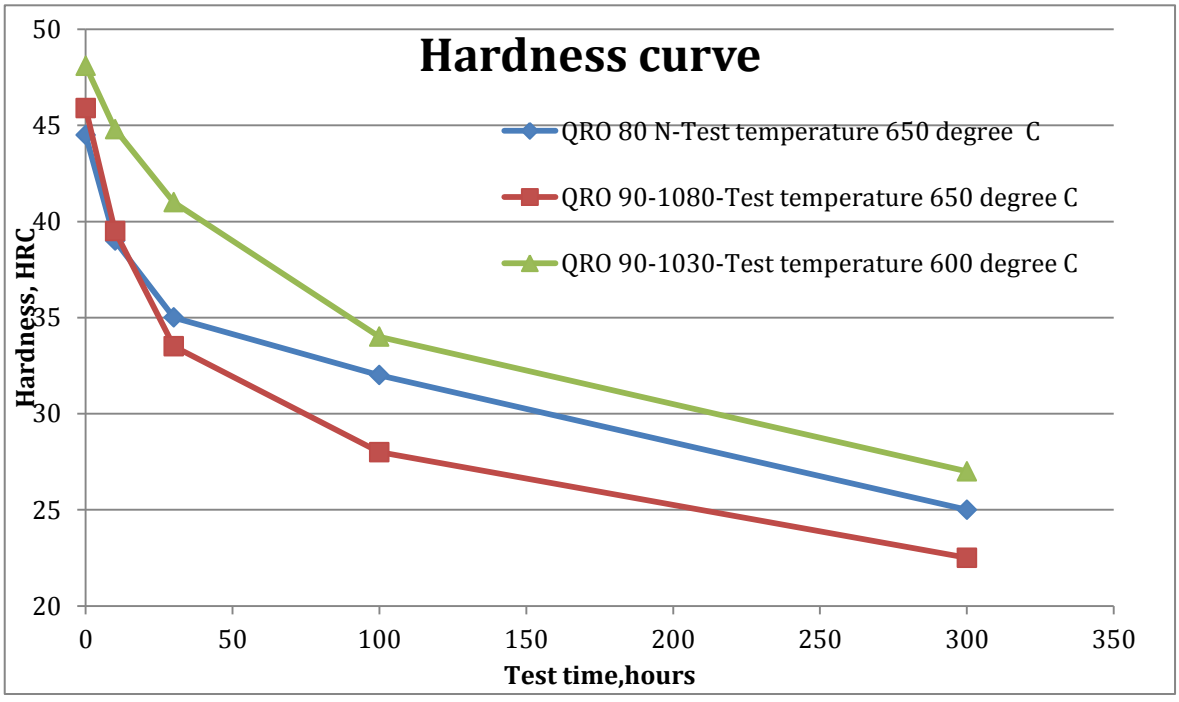

Figure 1: Hardness curve for materials used in this study [1].

1.2 Scope of this work

This work includes a comparative study of atom probe analysis of QRO 90 and QRO 80N hot work tool steels. The effect of secondary hardening and growth of carbides is a consequence of the different tempering temperature and hours. Annealing resistance tested (ART) samples (30h) were used to understand the behavior of the growth of carbides in comparison with samples tempered at 1 hour, representing the tool before usage.

One of the primary focuses of this work is also to identify the impact of nitrogen on secondary hardening.

Four samples, two of QRO 80 N and two of QRO 90 with different tempering times were analyzed. The details are given in table 2.

1.3 Heat treatment

The hot work tool steel is processed by different heating methods in order to produce a fine microstructure of martensite and carbides. This fine microstructure should favor different strengthening mechanisms used to harden the tool steel.

Soft annealing is one of the heat treatments applied to get a ferrite matrix with spheriodized carbides. It is achieved by heating the sample up to a temperature (around 850^{o}C); just above the A1-temperature i.e start temperature for austenitization. This helps the material to dissolve the carbides and shape them into spherical structure in order to produce a fine or even microstructure considering carbides.

Prior to soft annealing, the material is also processed through step annealing and regeneration annealing to get a smooth microstructure. QRO 90 has been soft annealed at 820^{o}C.

After soft annealing the material is hardened by increasing the temperature to fully austenitic range (i.e 1000^{o}C to 1200^{o}C). A complete transformation of BCC to FCC is achieved in order to fully dissolve the carbides and absorb the carbon and alloying elements into the matrix. After homogenizing the material, it is quenched i.e the material is cooled rapidly. It results in the formation of body centered tetragonal structure BCT. This is a fast process and due to the limited diffusitivity of carbon inside the matrix the carbon atoms are trapped inside the matrix. This gives a lath like structure known as ‘Martensite’.

Fresh martensite is very hard and brittle. To be used as a tool, the material needs to be softer and more ductile. Thus, it is processed through tempering treatments.

Hot work tools steel is usually tempered at 500^{o}C to 600^{o}C. The carbon and the alloying elements leave the matrix to produce a dense precipitation of carbides. This produces a hardening effect on the material also called ‘secondary hardening’.

1.4 Precipitation hardening

The strengthening mechanism depends on the resistance of a material to plastic deformation on the application of a load. It highly depends on the mobility of dislocations inside the material. Reducing the motion of the dislocations can enhance the mechanical strength of a material. Precipitation hardening is one of the important processes for hardening of hot work tool steel.

The primary strengthening is achieved by producing a solid solution with alloying elements. The next step is supersaturation of solid solution and the precipitation of secondary particles. This is usually done by a suitable heat treatment. The secondary precipitates stop the motion of dislocations resulting in an enhancement of tensile strength.

If the particles are small and coherent then the dislocation can cut through the particles. On the other hand if the particles are hard and strong then the dislocation puts a closed loop around the particles following Orowan's mechanism. For hot work tool steel, the particles are hard and strong. Orowan's looping is the dominant process as shown in fig 2.

The Orowan's shear strength is given by equation 1: [6]

$$\tau_y = 2\,G\,b/\,L \qquad (1)$$

where,

τ_y = Orowan's shear strength

G = shear modulus of the matrix

b = burger vector

L = interparticle distance

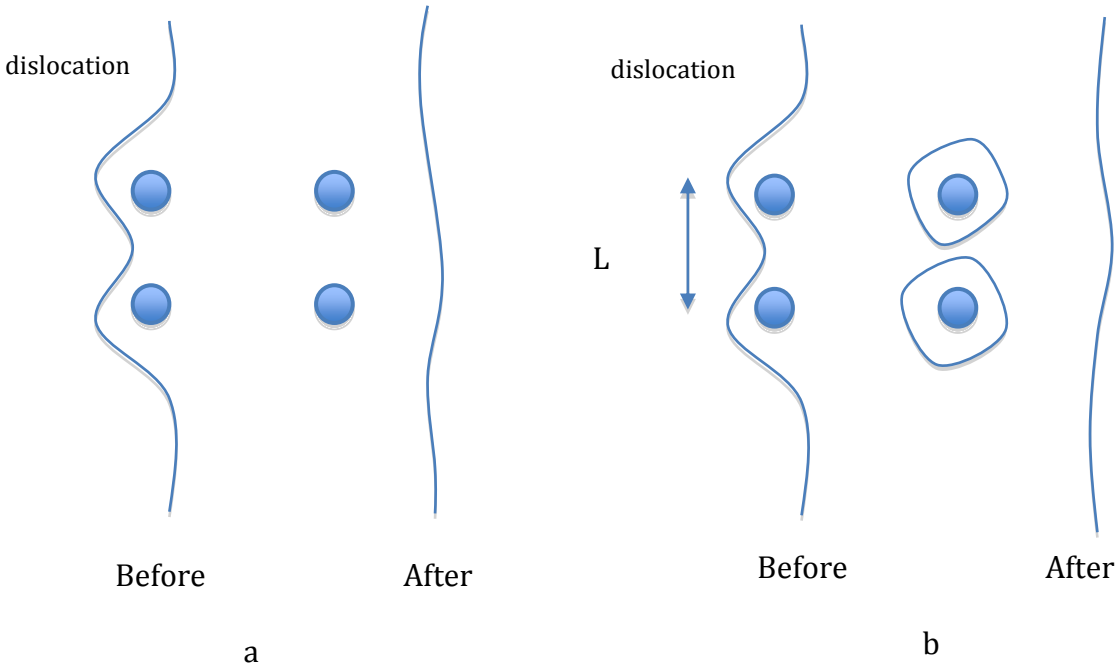

Figure 2: Orowan's mechanism; (a) the dislocation passes through the particles as they are small and coherent, (b) the dislocation passes through the particles by making a loop around them.

2. Experimental

2.1 Material

The chemical composition of the materials used in this study is given in table 3 and the heat treatments applied on the materials are given in table 2, together with the resulting hardness.

Table 2 Heat treatments applied on the materials.

S.N	*Sample*	*Austenitizing*	*Tempering*	*HRC*
1.	QRO 80 N	1100^{o} C/30 min	630^{o} C /2x2h +650^{o} C /1h	44.5
2.	QRO 80 N ART	1100^{o} C/30 min	630^{o} C /2x2h +650^{o} C /30h	35
3.	QRO 90	1030^{o} C/30 min	625^{o} C /2x2h	48.1
4.	QRO 90 ART	1080^{o} C/30 min	650^{o} C /2x2h +650^{o} C /30h	34

Table 3 Chemical composition of the materials used. (wt. %)

Material	*C*	*Si*	*Mn*	*Cr*	*Mo*	*V*	*N*
QRO 80 N	0.38	0.28	1.07	1.67	2.74	1.15	0.044
QRO 90	0.38	0.3	0.75	2.6	2.3	0.9	-

2.2 Atom Probe Tomography

Atom probe tomography (APT) works on the principle of field evaporation and mass spectrometry. Ions are field evaporated from the surface of a sample with the help of a high voltage, which produces a high electric field. A positive dc voltage is put on the sample. A short negative voltage is then applied to a local electrode in front of the sample. This pulse is usually 15-20 % of the dc voltage. The dc voltage is controlled so that field evaporation occurs only when the pulses are applied. After field evaporation, the positive ions are accelerated by the field. A few microseconds later they hit the position-sensitive detector. With the help of time of flight mass spectrometry (i.e from the time ions leave the surface to the time ions are detected) a relative mass to charge ratio is calculated to identify the ions using equation 2. The evaporation field used for materials in this work was 33 V/nm.

The potential energy of the ion (neV) is converted into kinetic energy ($\frac{1}{2}\ mv^2$) by field evaporation of the specimen ion. As an approximation, the velocity of the ion becomes constant. It reaches the terminal velocity within a few radii of the tip. Using $v = d/t$ the mass-to-charge ratio can be calculated as:

$$m/n = 2\ e\ V\ t^2 / d^2 \qquad (2)$$

Where

m = mass of the ion

n = charge number on the ion

e = charge of the electron

d = flight distance.

t= time of flight

V = total applied voltage on the specimen

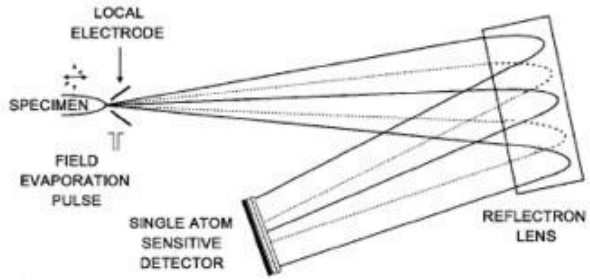

Figure 3: The working mechanism of atom probe with the use of a reflectron [9].

There are some energy deficits that result due to the incapability of transforming the complete potential energy of the ion into kinetic energy. The energy deficits are due to the evaporation process or voltage fluctuations. It results in broadening of peaks in the mass spectrum. This problem is overcome using energy compensation i.e an electrostatic lens called 'reflectron lens' [7]. The use of a reflectron improves the mass resolution by a factor of 10. The working mechanism of the atom probe is illustrated in fig.3.

In the LEAP 3000X HR, instead of voltage pulsing laser pulsing can be used to field evaporate ions from the surface, by increasing the temperature during a few nanoseconds. A micro-positioning specimen stage is aligned with the local electrode with the help of two long-range optical microscopes. Final alignment is done using the field-evaporated ions and their hit map on the detector.

Recorded data is used to form a three-dimensional tomographic reconstruction of the sample. This is called '3-D atom probe'.

A Local electrode atom probe (Imago: LEAP 3000X HR) is used for analysis. Some features of the LEAP are given below:

- The detector efficiency is 37% with a mass resolution of 1/1000. The spatial resolution is 0.3 nm and the dead time of the delay line detector is less than 3 ns [8].
- Large magnification nearly 5 millions times (tip radius of 50 nm to 40 cm distance from tip to detector with image compression factor of 1.65).
- Due to multiple hits and the dead time of the detector there is an inefficiency of measuring some ions, for example giving too low a carbon concentration. Results can be made better by using ^{13}C method [8].
- 250 000 atoms per atomic layer can be collected due to the large field of view [9].

2.3 Sample preparation

The starting sample in the atom probe is a needle shaped metal called 'blank'. It is transformed in to a smooth tip by an electropolishing process. The tip of the final specimen has a circular cross-section with a radius of 10-100 nm.

The specimen should always be checked for magnetization, oxidation layers or rust. The specimen can be demagnetized with the help of a rotating magnet. The oxidation layer or rust can be removed by rubbing the specimen on a thin carbon paper.

There are different sample preparation methods and techniques. For metals, electropolishing can be used for sample preparation.

- **Electropolishing:**

Materials with good electrical properties can be electro-polished. It is a two-step process. In the first step, the specimen is pushed into an Al-holder and clamped using a pair of pliers. The specimen holder is connected with the positive side of a voltage supply so it works as anode. The negative terminal holds a gold cathode in the form of a ring as shown in fig.4. A beaker is filled with inert 1,1,2-triclortrifluorethane then a thin layer of electrolyte (70% alcohol, 20% Glycerol, 10% perchloric acid) is poured to float on top of it.

The voltage is set between 20-25 V in order to produce a neck in the blank. It is usually a fast process and care should be taken to control the process by a switch. The blank is moved up and down, in order to prevent attack on the air-electrolyte interface.

In the second step, the electrodes are placed in fresh 2% $HClO_4$ in 2-butoxyethanol. The voltage is set between 15-20 V. After some time the blank breaks off at the neck providing two sharp tips as shown in fig.4. Now the needle has a tip radius of typically 50 nm. The remaining part of the blank is also pushed in to a specimen holder. Both tips are washed with ethanol, dried and analyzed in the optical microscope. In some circumstances, SEM can be used for better imaging of the tip as shown in fig.5.

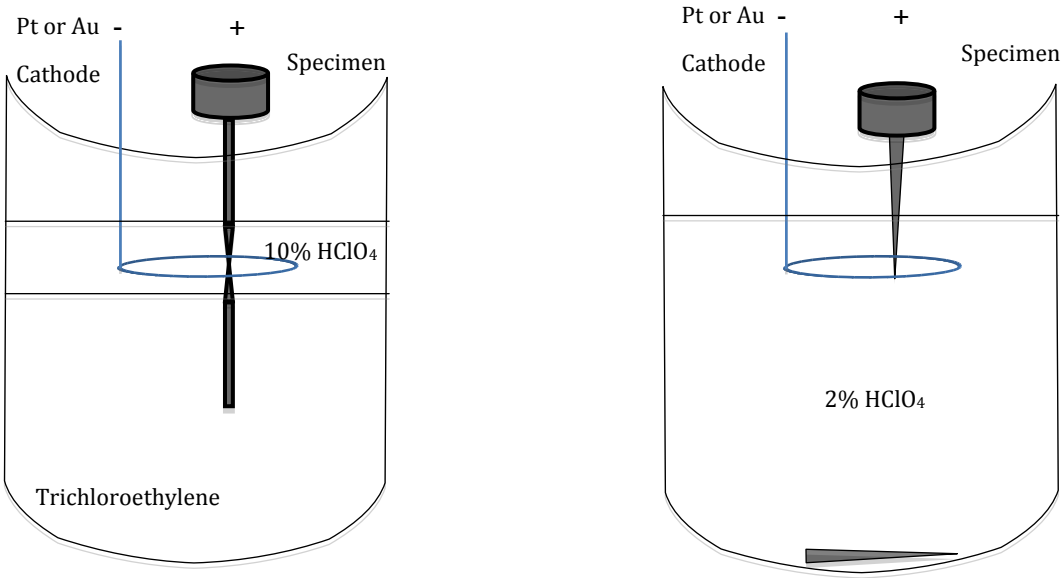

Figure 4: Two step Electropolishing: first step (left) to produce a neck in the blank; second step (right) to produce two sharp needles.

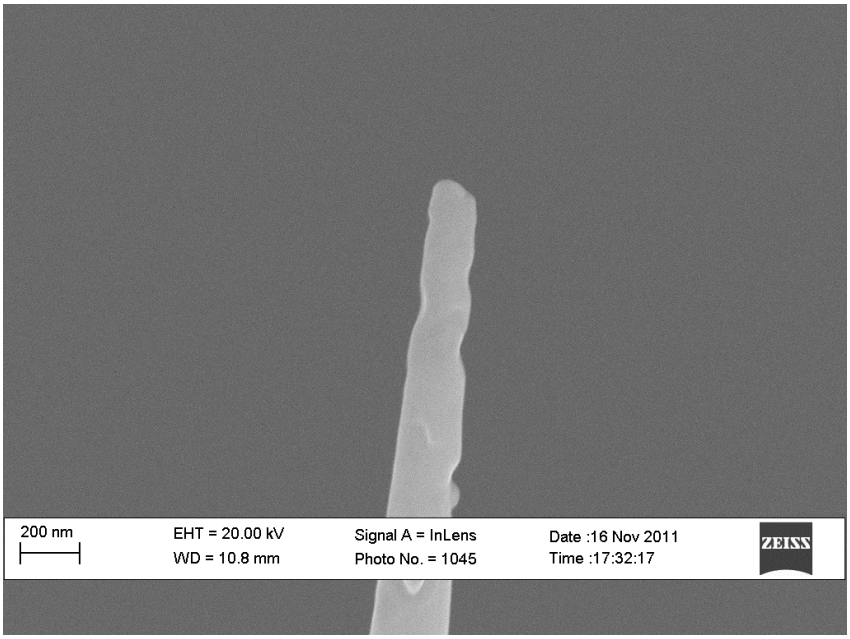

Figure 5: SEM image of the sample's tip showing the tip's radius to be around 100 nm. [SEM (Leo Ultra FEG)]

2.4 General Data Evaluation

In atom probe, the ions are detected by time of flight and identified with mass to charge ratio. The ion distribution collected with a position-based detector is reconstructed to form a tomographic image of the sample with the help of a computer software (IVAS 3.4.3).

2.4.1 Mass spectrum analysis:

The ions collected are evaluated as a mass spectrum. It is a graph of number of counts detected versus mass-charge ratio. After identification, these peaks are labeled with the appropriate element (or ion).

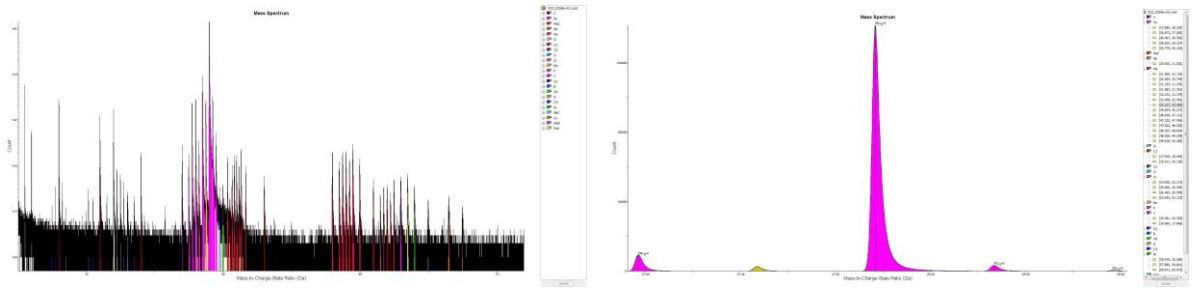

Figure 6: An image of a mass spectrum from IVAS. 3.4.3 (left). Closer view of the highest peak of Fe^{++} and its isotopes (right).

Sometimes, the identification can be very confusing due to overlap of peaks. The assignment of the peaks can be further improved by doing a comparison of natural percentage abundance of elements and its isotopes. Fig.6 illustrates the natural abundance of $^{56}Fe^{+2}$ and its isotopes.

2.4.2 Overlap of peaks:

Some peaks overlap due to having the same mass-charge ratio. They are further investigated, comparing the ion concentration of their relative isotopes (i.e the comparison of observed peak's height with the expected concentration or a comparison of peaks observed with number of isotopes of a particular ion). Overlap peaks can also be decomposed in to its constituents through the IVAS.3.4.3.

The program decomposes the peaks based on the natural abundance of the isotopes, then extracts the right amount of ions of different isotopes lying under one peak. This enhancement is very useful to get more accurate results.

- **Overlap of nitrogen and silicon peaks:**

Silicon (Si^{++}) and nitrogen (N^{+}) peaks overlap as shown in fig.7. They are further investigated by comparing the concentration of their relative isotopes.

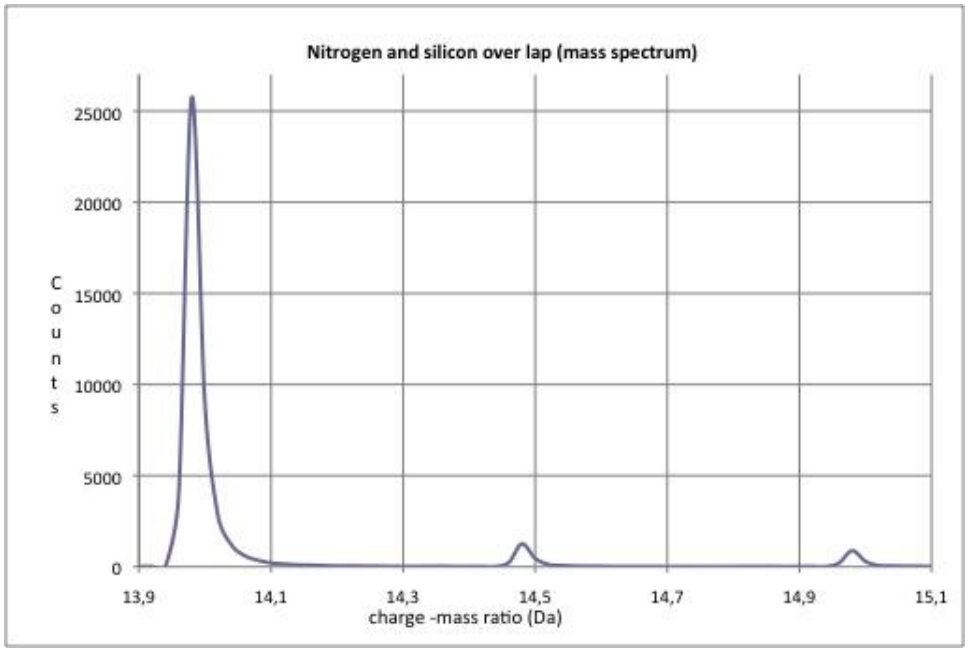

Figure 7: Region of overlapping between Si^{++} and N^{+}.

The mass spectrum above shows the 14-peak, the 14.5-peak and the 15-peak. If these peaks would have been completely nitrogen peaks then there would not be a center peak (≈14.5) because nitrogen does not contain an isotope of mass-charge ratio of approximately 14.5. Comparing the available ion concentration of silicon and its isotopes (within log scale) as shown in the fig.8.

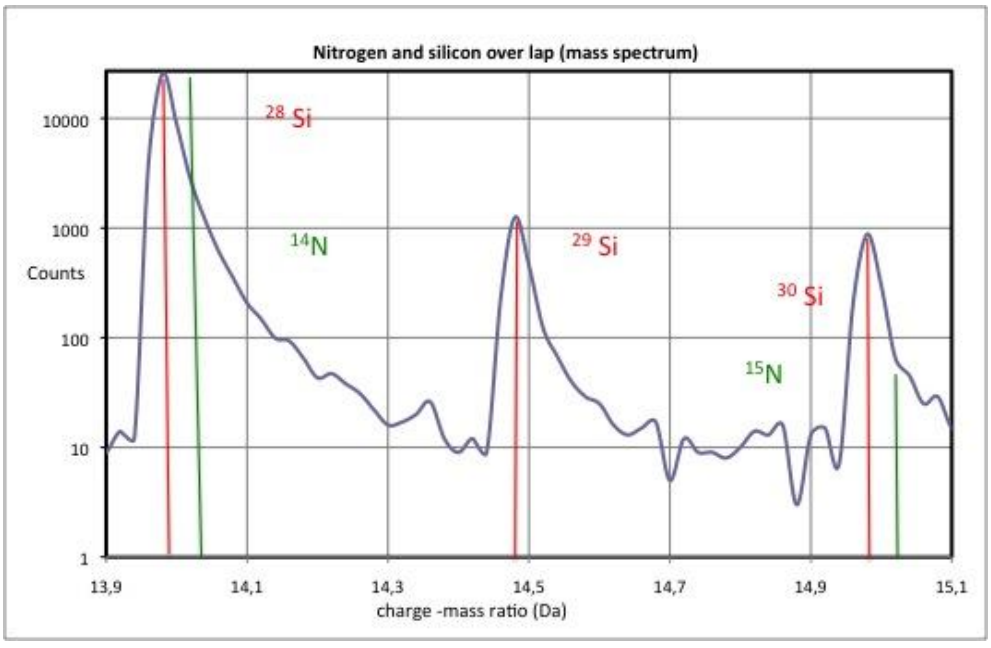

Figure 8: Overlap region in log scale showing the expected counts of isotopes of Si^{++} and N^{+}.

It is evident that the silicon isotopic abundance fulfills the recorded concentrations of the three peaks. Table 4 shows that the Si expected counts match with the counts from the peak whereas nitrogen's expected counts do not fulfill the observed counts. Hence, it

can be easily concluded that nitrogen-14 is recorded in very small quantity or almost in negligible amounts.

Table 4 Comparison of observed counts from the peaks to expected counts from isotopic abundance.

Isotopes	^{28}Si	^{29}Si	^{30}Si	^{14}N	^{15}N
Expected counts		2232	1482		159
Natural abundance	92.2 %	4.67%	3.10%	99.60%	0.36%
Counts from peak	44077	2259	1537	44077	1537

- **Overlap of Mo, Cr, MoC, MoN and Fe peaks:**

Fig.9 shows a part of the spectrum that has several important peak overlaps. Certain parameters have to be considered in order to get a good identification of the peaks. Table 5 illustrates that the expected counts of Mo^{2+} are nearly the same as the observed and calculated values from the mass spectrum.

Comparing the pattern of the observed peaks of Mo, identifies the MoC peaks. This might include a complete comparison of the height of individual peaks of Mo and MoC sequentially. It can be seen from fig.10 that the six MoC peaks follow the same pattern as Mo except for the seventh peak (^{100}M). It has a bigger height compared to the previous MoC peaks; this last peak is identified to be Fe^{+}. It also fulfills the expected counts of Fe^{+}.

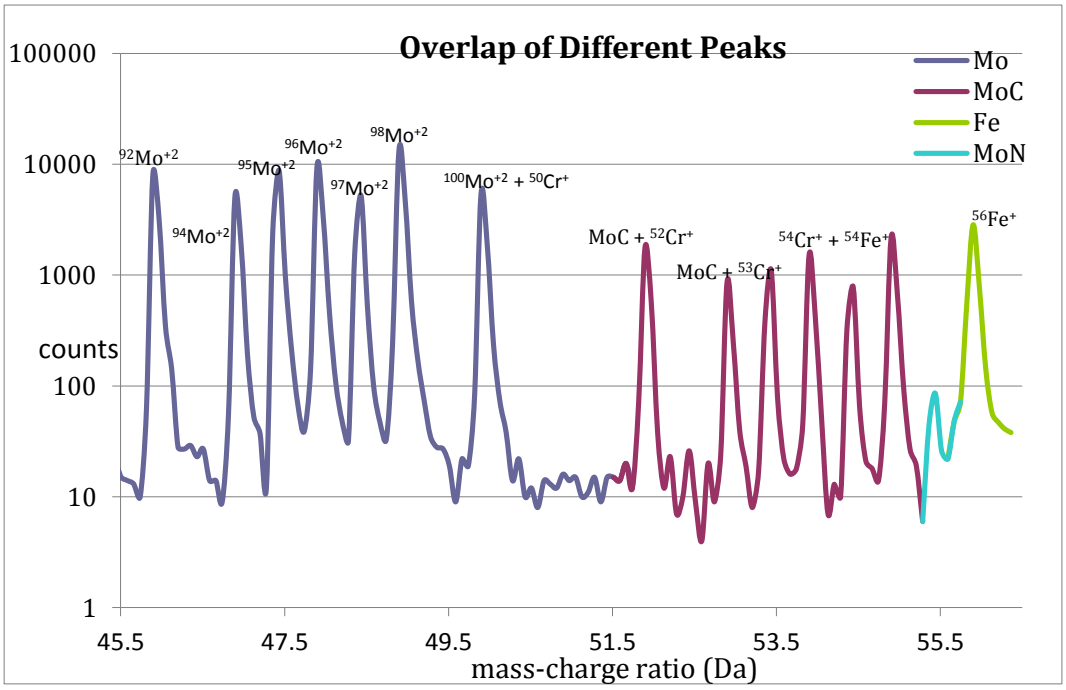

Figure 9: Mass spectrum: Overlap of Mo^{++}, Cr^{+} and Fe^{+} peaks in log scale.

Some peaks of MoC are also overlapping with Cr^{+} peaks. Table 6 and table 7 show that the expected counts of Cr^{+} and Fe+ do not fit with the observed counts. There is a very small peak at 55.5 Da between the ^{56}Fe+ and ^{98}MoC peak, it is considered to be MoN.

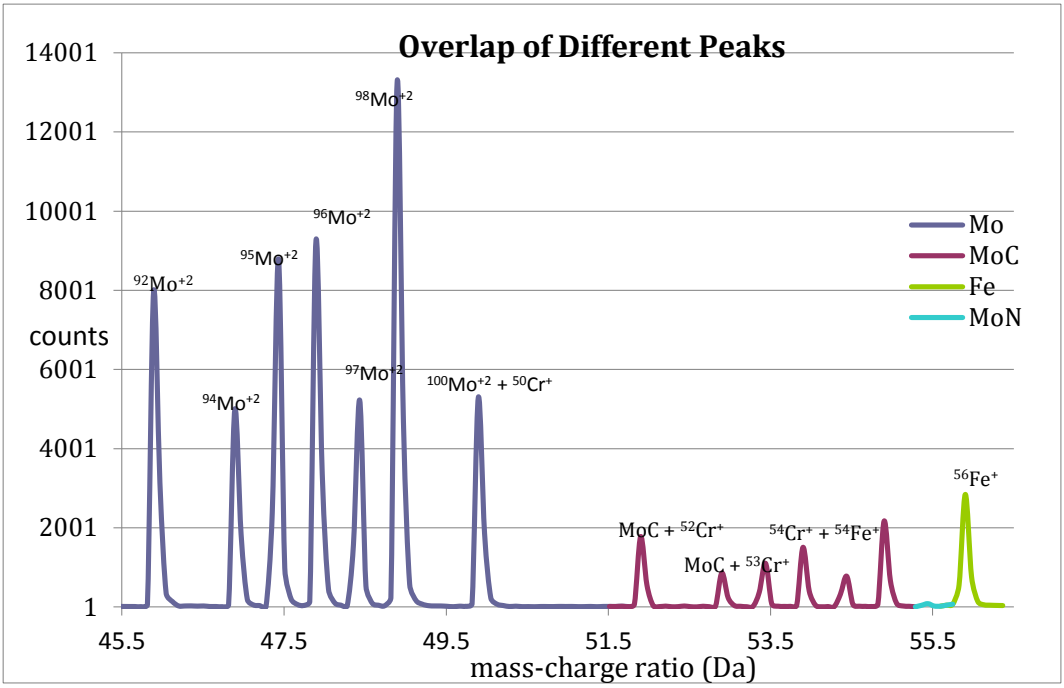

Figure 10: Mass spectrum: Overlap of peaks of Mo^{++}, Cr^{+} and Fe^{+}.

Table 5 Comparison of expected counts from the isotopes of Mo^{++} to observed counts from the peaks.

Mo peaks	$^{92}Mo^{+2}$	$^{94}Mo^{+2}$	$^{95}Mo^{+2}$	$^{96}Mo^{+2}$	$^{97}Mo^{+2}$	$^{98}Mo^{+2}$	$^{100}Mo^{+2}$
Expected counts	11662	7270	12512	13109	7466		7568
Natural abundance (%)	14.84	9.25	15.92	16.68	9.55	24.13	9.63
Counts from peak	11611	7030	12380	13224	7434	18964	7546

Table 6 Comparison of expected counts from isotopes of Cr^{+} to observed counts from the peaks.

Cr peaks	$^{50}Cr^{+}$	$^{52}Cr^{+}$	$^{53}Cr^{+}$	$^{54}Cr^{+}$
Expected counts	125.0		273.3	68.0
Natural abundance (%)	4.34	83.78	9.50	2.36
Counts from peak	7546	2410	1915	1915

Table 7 Comparison of expected counts from isotopes of Fe^{+} to observed counts from the peaks.

Fe peak	$^{54}Fe^{+}$	$^{56}Fe^{+}$	$^{57}Fe^{+}$
Expected counts	274.7		99.1
Natural abundance (%)	5.84	91.75	2.11
Counts from peak	1915	4312	4215

2.4.3 Different range files:

The assignment of peaks to ions is called a range file. The ion distribution changes for each part of the reconstruction. Therefore the mass spectrum needs to be analyzed for different regions of the reconstruction and a unique range file is saved for each region to be used in

IVAS 3.4.3. This has particular significance as it gives the correct concentration of ions in a particular region (such as matrix, carbide, retained austenite).

2.4.4 One-dimensional concentration profile:

One-dimensional profile is a tool to study the different interfaces within the analysis or to find the concentration of elements in a particular region.

Different region of interest (ROI) objects can be selected in the software; cylinder, cube or sphere. They are used to analyze a particular region inside the tomographic reconstruction. The ions contained in the ROI (cylinder) can be extracted from the complete reconstruction and analyzed separately. This is shown in fig.11. The ROI can construct one-dimensional profile of ions inside the cylinder. It is used to know the change of concentration of ions inside a particular region (e.g carbide).

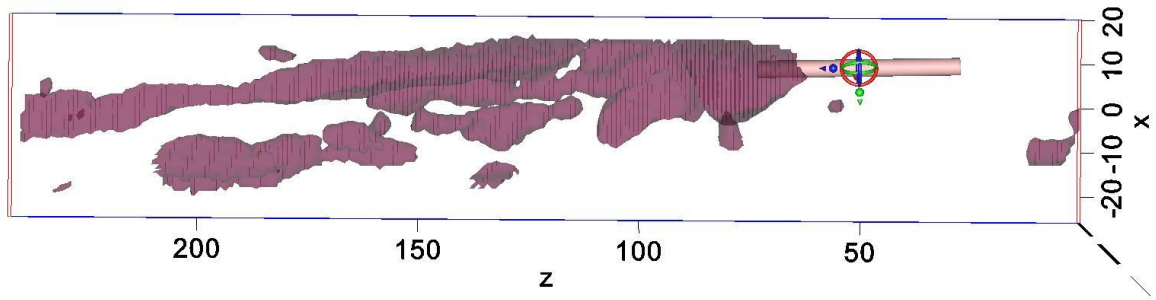

Figure 11: The use of ROI (cylinder) to construct one-dimensional concentration profile of ions.

2.4.5 Interfacial study with the help of iso-surface (proxigram):

A proxigram (from proximity histogram) is a concentration-distance graph that represents the concentration of elements at an interface and the nearby region. By making an iso-concentration-surface (isosurface) of a particular element (or several elements), a proxigram can be made. The zero distance in the proxigram shows the interface, positive distances show the region inside the interface while negative distances show the concentration of elements outside the interface. Different proxigrams can be taken to analyze the presence of elements at interfaces between different regions.

3. Results And Discussion

3.1 QRO 90

3.1.1 Tomographic Reconstruction:

Several samples were investigated through atom probe but the presented results are gathered from two successful runs. The measurements were performed at laser pulsing mode with laser energy of 0.3 nJ, frequency of 200 kHz and the specimen temperature of 56 K for Run 2580, 76 K for Run 2579. Few millions counts were recorded. Fig.12 and fig.13 show the tomographic reconstruction of the samples. Table 8 shows the bulk composition of QRO 90.

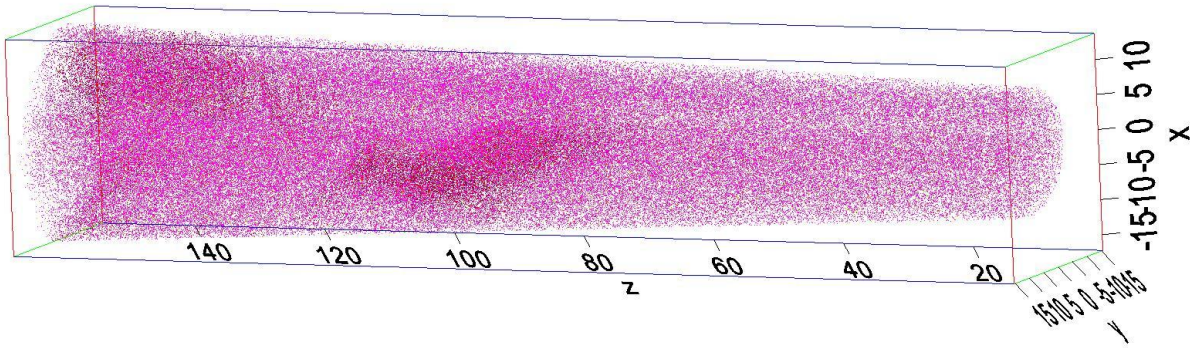

Figure 12: Tomographic reconstruction from run 2579 (25x30x140 nm). (Fe ions in pink color while the dark regions are carbides with Mo, V and Cr ions).

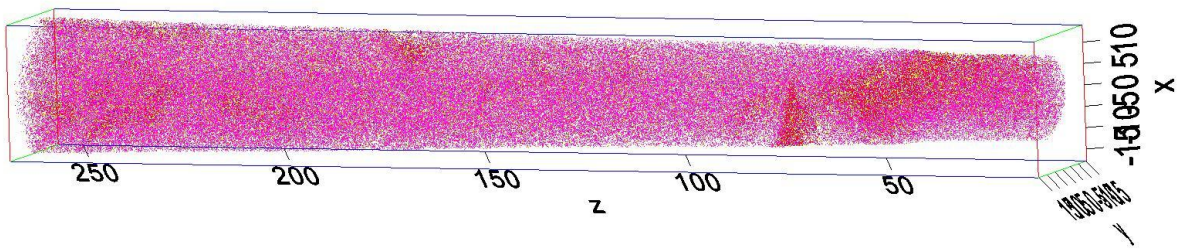

Figure 13: Tomographic reconstruction from run 2580 (20x20x250 nm). (Fe ions in pink color while the dark precipitates are carbides with Mo, V and Cr ions).

Table 8 Concentration (at.%) of elements present in the bulk.

Elements	*Ions*	*At %*
Fe	4023654	92.8
Cr	95974	2.2
Mo	47360	1.1
C	37993	0.9
Si	30191	0.7
Mn	26689	0.6
V	21471	0.5
Ni	13207	0.3
N	203	0.005
Total ions	4333038	

3.1.2 Carbides:

Fig.14 and fig.15 show images of iso-concentration surfaces of Mo, V and C. Most of the carbides are small with a few hundred ions having an equivalent radius < 1.4 nm. There are also traces of big carbides but in small numbers as presented in table 9.

High temperature during austenitizing can dissolve more alloying elements in the matrix and can produce less coarsening of secondary carbides. Following table 9, the carbides are considered to be MC type with enrichment of Mo and high solubility of V. The atom probe has bad measurement statistics for carbon around 10-15% lower than expected. Thus the carbon concentration is believed to be around 50%.

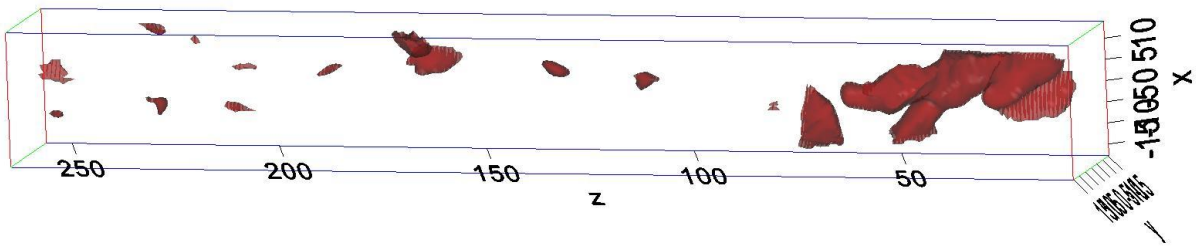

Figure 14: Iso-surface of Mo, V and C from run 2580 (20x20x250 nm).

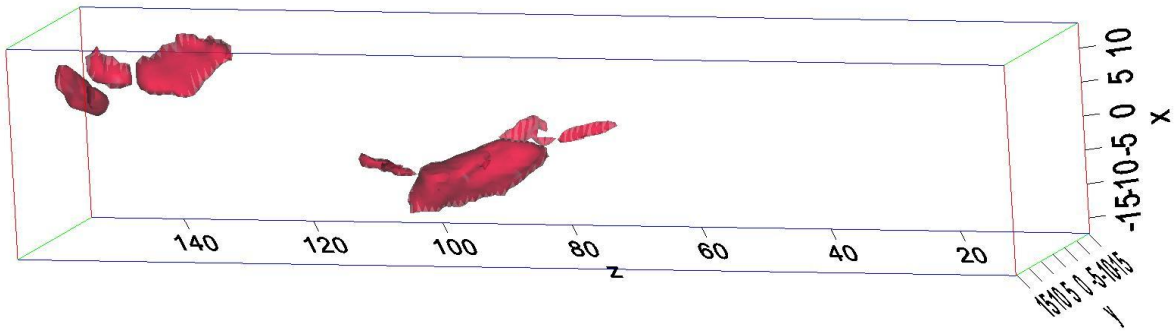

Figure 15: Iso-surface of Mo, V and C from run 2579. (20x20x250 nm)

Table 9 Composition of carbides (at.%) and their approximate equivalent size.

Run 2580	*C*	*Mo*	*V*	*Fe*	*Cr*	*Total Ions*	*Radius (nm)*
MC	33.2	29.6	13.2	11.8	9.3	40388	6.1
MC	33.5	28.4	15.6	9.5	9.2	4621	3.0
MC	33.0	23.0	18.9	12.7	8.0	1530	2.1
MC	35.2	22.8	21.3	2.6	7.4	492	1.4
MC	25.6	21.1	16.6	19.8	9.9	358	1.3
MC	38.6	18.1	29.9	1.9	6.0	279	1.2
MC	42.1	18.9	18.7	4.5	7.8	260	1.1
MC	21.4	22.4	18.3	23.5	5.2	124	0.9
MC	35.5	15.7	9.8	19.0	8.9	119	0.9
MC	35.3	30.2	11.2	8.1	7.6	106	0.8
MC	47.2	16.8	16.1	3.7	6.8	105	0.8
MC	51.2	21.1	15.8	2.7	5.9	93	0.8
MC	45.7	14.2	15.5	13.6	4.9	57	0.7
MC	37.9	18.7	26.9	11.2	-	32	0.6
Run 2579							
MC	37.7	26.0	22.6	2.5	8.8	5897	3.2
MC	36.0	25.6	21.2	3.2	10.7	1639	2.1
MC	38.5	26.9	22.4	1.5	7.9	716	1.6
MC	33.5	25.5	22.3	1.5	9.4	307	1.2
MC	45.4	23.3	14.6	2.8	9.7	143	0.9
MC	31.5	22.3	22.1	2.1	14.7	134	0.9
MC	49.7	14.0	19.0	1.4	8.4	99	0.8

3.1.3 Martensite-carbide interface:

Fig.17 shows the change in concentration of elements at martensite-carbide interfaces. There is an enrichment of low concentration alloying elements like Al, Co, P, Cu and Ni at the interface. A small quantity of nitrogen is also found near the interface and inside the carbide. Fig.16 shows the distribution of high concentration ions near the interface and

shows that the carbide is a mixture of C, Mo and V with some amount of Cr and Mn as well. Comparing table 8 and table 10, it can be estimated that most of the Mo and V has dissolved inside the carbides.

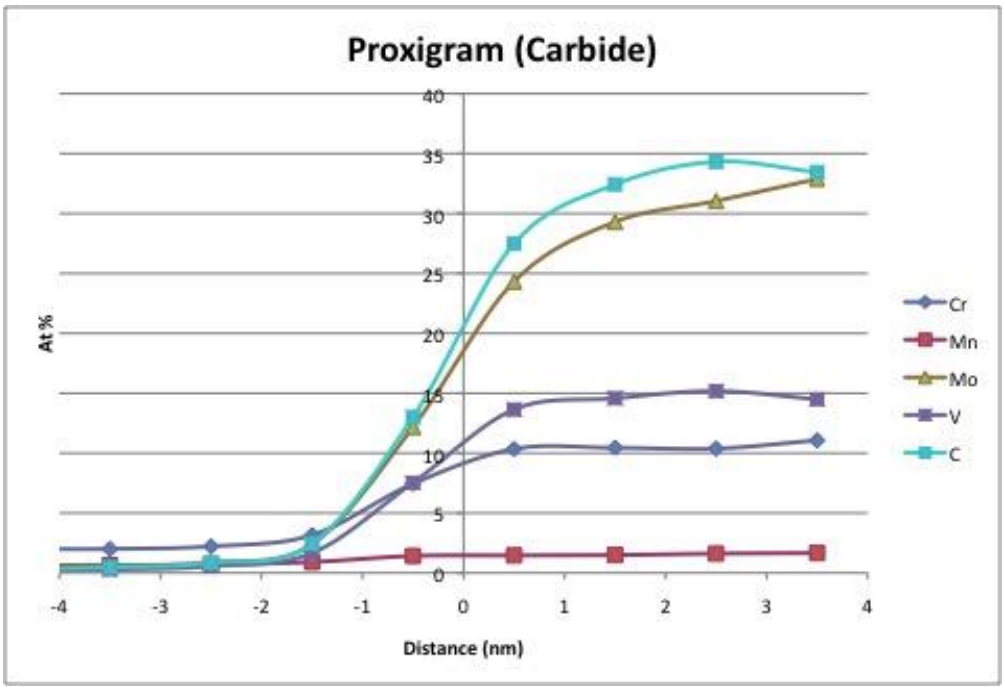

Figure 16: A proxigram of carbides showing high enrichment of Mo, V and Cr.

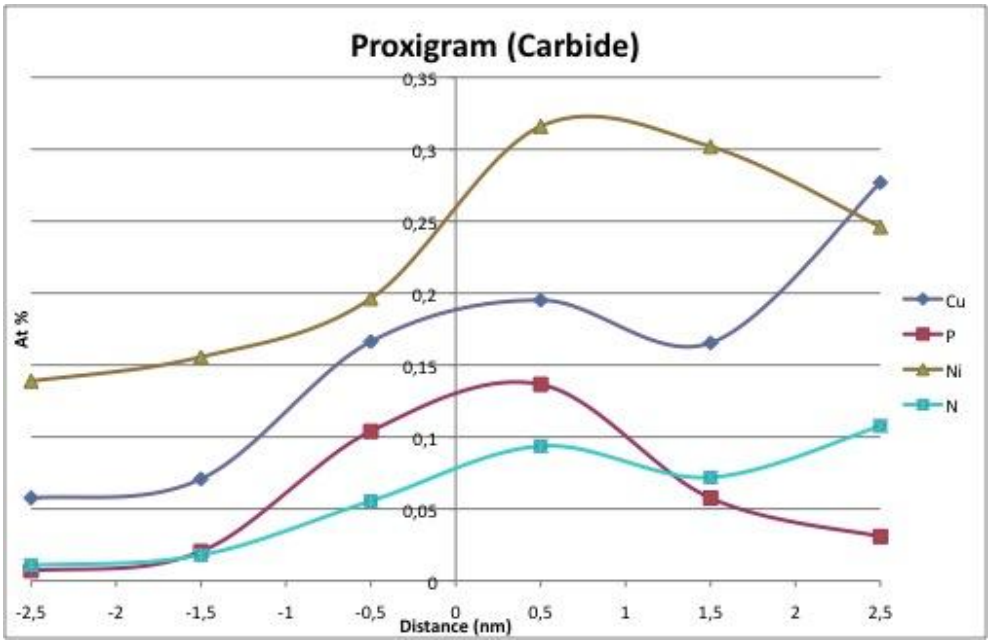

Figure 17: A proxigram of carbides showing traces of low concentration elements near the interface.

Table 10 Composition of matrix. (at.%)

Elements	*Ions*	*At %*
Fe	3991141	94.0
Cr	89857	2.1
Si	29646	0.7
Mo	29376	0.7
Mn	26571	0.6
C	17483	0.4
Ni	13053	0.3
V	12670	0.3
Total Ions	4244976	

3.2 QRO 80 N

3.2.1 Tomographic image:

Several samples were investigated using the atom probe, and the results from two samples are presented here. The measurements were performed at laser pulsing mode with laser energy of 0.3 nJ, frequency of 200 kHz and the specimen temperature of 54 K for Run 2556, 56 K for Run 2557. A few million counts were recorded. Fig.18 shows the tomographic reconstruction of the sample with a dimension of 40x40x250 nm.

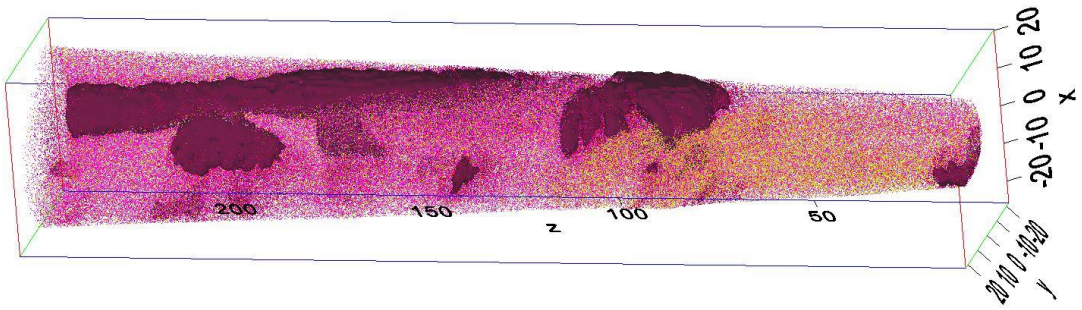

Figure 18: Tomographic image showing martensitic matrix (pink color) and carbides (dark brown patches), indicated by isosurfaces.

Table 11 shows the concentration of different elements contained in the entire analysis. It shows that it has a low alloying content, less than 10 at.%.

Table 11 Concentration (at.%) of elements in the bulk.

Ion type	*Count*	*At %*
Fe	7251689	91.3
Cr	145413	1.8
C	134949	1.7
Mo	130185	1.6
Mn	125099	1.6
V	84567	1.1
Si	47878	0.6
N	994	0.012
Total Ions	7920774	

3.2.2 Carbides:

Fig.19 and Fig.20 show tomographic reconstructions of carbides inside the analyzed volume. The carbides are visualized by creating an iso-surface of the sum of Mo, V and C. The carbides look bigger than their real size due to local magnification effects. The lower density regions (carbides) appear to be bigger than the real size. Alternatively, the high density region (matrix) seems to be compressed.

The carbides in QRO 80N seem to be more coarse at 1hr as compared to QR0 90.The difference in coarsening is due to the fact that the QRO 90 has higher austenitizing temperature and tempered twice at 625^{o} C where as QRO 80N was tempered two times at 630^{o} C and one time at 650^{o} C.

Table 12 present the concentration (at.%) of the carbides and their approximate equivalent radius. It can be seen that some precipitates are bigger in size having an approximate radius in the range of 5-8 nm. This type of precipitation can be a result of the presence of retained austenite (discussed in detail in later part of the report).

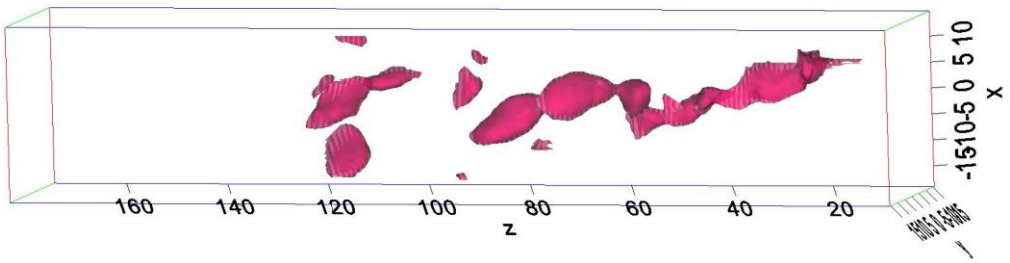

Figure 19: Run 2557, iso-surface of Mo, V and C (carbide) inside the matrix. (25x30x170 nm)

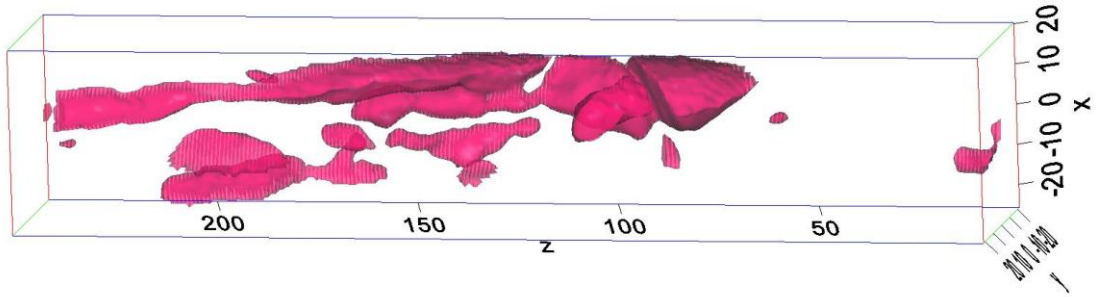

Figure 20: Run 2556, iso-surface of Mo, V and C (carbide) inside the matrix (40x40x250 nm).

Table 12 Concentration (at.%) of elements found inside the carbide and their approximate equivalent radius.

2556	*C*	*Mo*	*V*	*Cr*	*Fe*	*N*	*Total counts*	*Radius (nm)*
MC	37.8	32.7	20.1	6.4	1.3	0.5	84852	7.9
MC	39.7	29.2	21.1	6.4	1.5	0.5	59708	7.0
MC	39.4	29.1	22.2	5.2	1.7	0.5	49491	6.6
MC	39.6	28.3	21.7	6.5	1.7	0.6	34378	5.8
MC	43.3	27.7	19.8	5.2	1.1	0.3	4901	3.0
MC	39.1	28.4	22.5	6.1	1.3	0.5	4087	2.9
MC	41.8	26.8	21.2	5.9	2.0	0.5	3154	2.6
MC	42.5	29.1	17.9	6.4	0.7	0.7	1804	2.2
MC	42.8	23.3	23.0	5.4	2.0	0.6	783	1.6
MC	41.1	32.3	17.5	4.3	2.3	0.1	630	1.5
MC	39.3	26.0	22.3	5.1	3.5	0.8	318	1.2
MC	53.9	24.2	16.3	0.8	0.5	0.6	228	1.1
MC	28.3	25.8	29.1	4.7	5.3	0.9	83	0.8
2557								
MC	40.6	27.9	21.3	6.1	1.8	0.6	4085	2.9
MC	41.3	27.3	20.5	5.3	2.7	0.6	3885	2.8
MC	39.7	28.7	22.0	6.4	0.7	0.6	3399	2.7
MC	35.6	28.2	24.4	6.2	2.8	0.7	2127	2.3
MC	40.0	28.0	23.6	6.1	0.6	0.6	1425	2.0
MC	37.1	28.9	22.9	6.5	2.2	0.8	1220	1.9
MC	34.8	28.7	24.6	7.3	1.1	0.8	430	1.3
MC	40.3	26.6	23.7	6.8	0.6	0.9	404	1.3
MC	39.9	23.3	24.2	8.0	-	2.2	86	0.8
MC	38.9	21.3	19.4	14.5	5.2	-	57	0.7
MC	39.3	20.6	26.2	5.0	-	-	57	0.7

3.2.3 Martensite-carbide interface:

Fig.22 shows the presence of Si and Mn at the interface. Fig.23 shows the presence of alloying elements like P, Ni, B and Nb at the interface. Nitrogen seems to be located at the interface and inside the carbide. With the aid of table 12, it is believed that most of the carbides are MC type with high concentration of Mo and V. Fig.21 shows the presence of elements that are highly enriched in the carbides like C, Mo, V and Cr.

The composition of the martensite is obtained by excluding the carbides (austenite regions is present) from the total volume. After mass spectrum analysis, a decomposition of peaks is done to get a good concentration of elements present in the martensite region. Table 13 shows the different concentration of elements present inside the martensite. It has a low carbon concentration and a low chromium content, less then 0.5 at %. It is a low chromium-low carbon martensite with morphology of lath like structure.

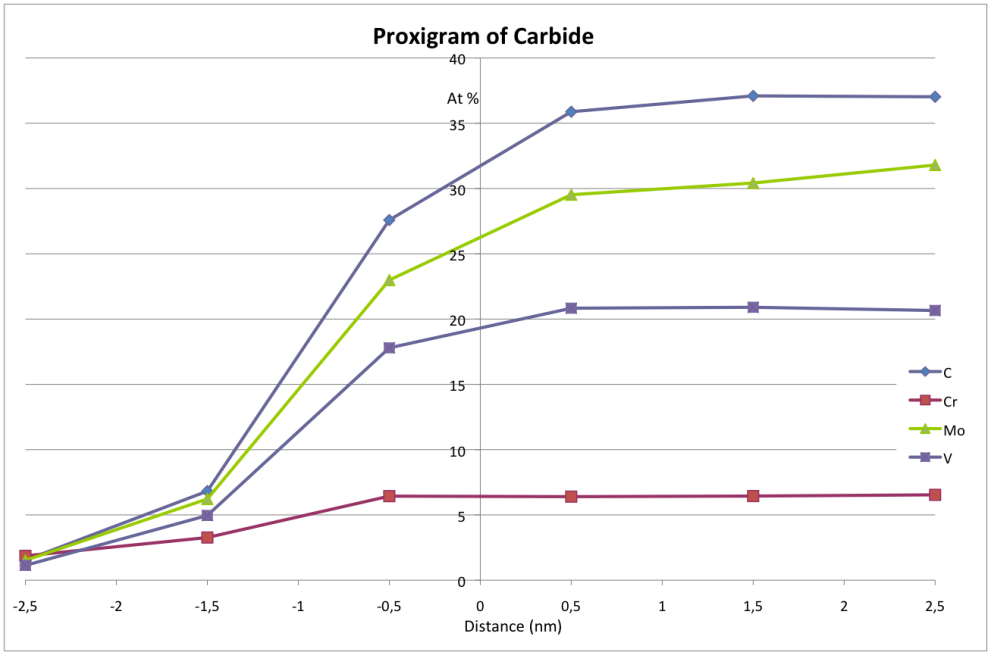

Figure 21: A proxigram of carbide-matrix interfaces showing the high enrichment of Mo, V and Cr.

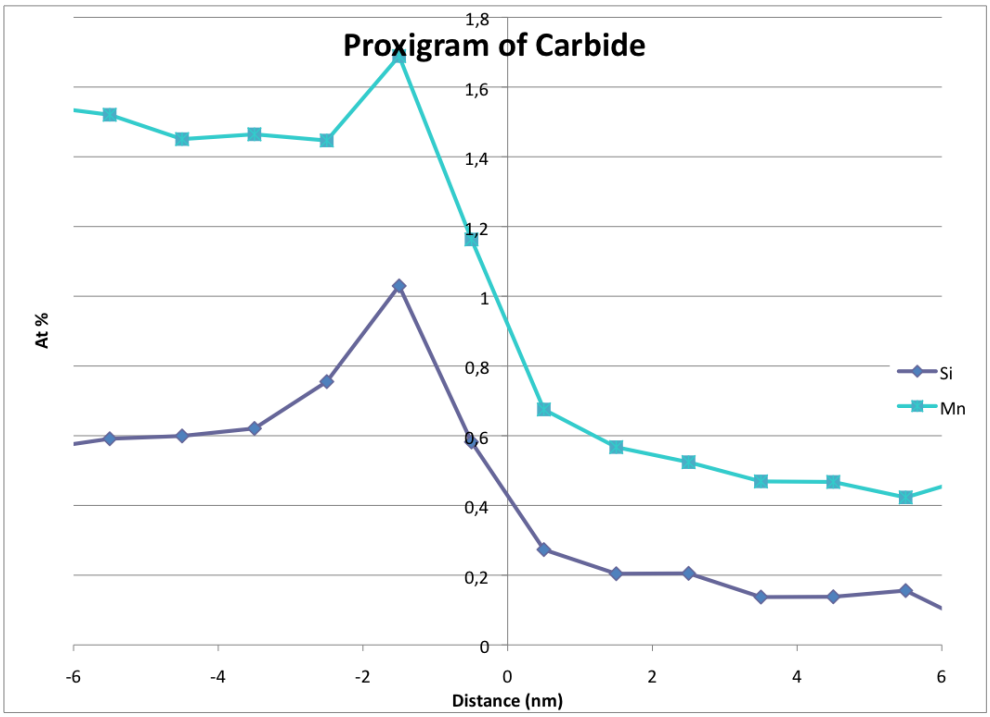

Figure 22: A proxigram of carbide showing high concentration of Si and Mn near the interface. The carbide is on the positive *x*-axis.

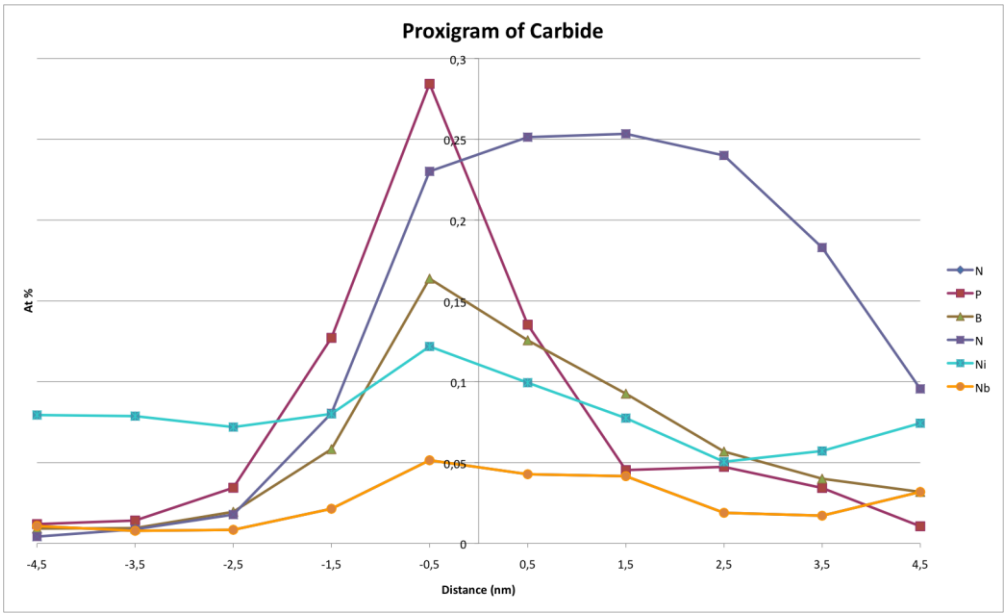

Figure 23: A proxigram of carbide showing traces of alloying elements near the interface.

Table 13 Concentration (at.%) of elements found inside the martensite.

Elements	*Ions*	*At %*
Fe	5631086	95.1
Cr	93009	1.6
Mn	66433	1.1
C	13734	0.2
Si	33028	0.6
Mo	26272	0.4
Ni	11057	0.2
V	9487	0.2
N	361	0.01
Total Ions	5884467	

3.2.4 Retained austenite:

The occurrence of retained austenite increases with carbon content in steels. With at.% of 0.77 carbon, the relative percentage of retained austenite could be 10-12 vol % [10]. The presence of retained austenite may be detrimental to the mechanical properties of the tool and might affect the tempering resistance. On application of stress, the retained austenite could form fresh untempered martensite resulting in a surface deformation. The formation of retained austenite can also be a consequence of adding nitrogen in the material [11].

Retained austenite was found in only one analysis. It had a surprisingly high concentration, 4.4 at.% of Mn as shown in table 14.

Table 14 Concentration (at.%) of elements found in retained austenite.

Elements	*Ions*	*At %*
Fe	985558	90
Mn	48761	4.4
Cr	23051	2.1
C	8486	0.8
Mo	8507	0.8
Si	7667	0.7
V	4357	0.4
Ni	2782	0.2
N	185	0.016
Total ions	1089354	

- **Retained austenite-carbide interface:**

Fig.24 shows a tomographic image of retained austenite and a carbide. The interface has very small enrichments of N, P and Si shown in fig.25. It is interesting to know that most of the nitrogen is dissolved inside the carbides or in retained austenite. Also, it seems to have a bit high concentration near the interfacial region.

Fig.26 shows one-dimensional concentration profiles across the austenite-carbide interface. It also shows a possible inhomogeneous concentration of Mo and V inside the carbide. The

Mo concentration is high inside the carbide towards the center and it decreases towards the interface of the carbide. The carbide seems to have high enrichment of V near the interfacial region.

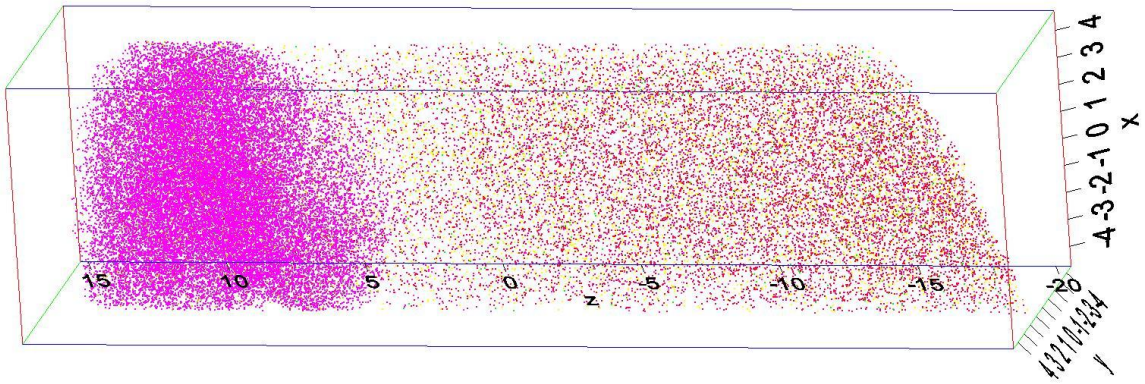

Figure 24: Tomographic image of interface between austenite and carbide (pink Fe, brown C, red Mo, yellow V).

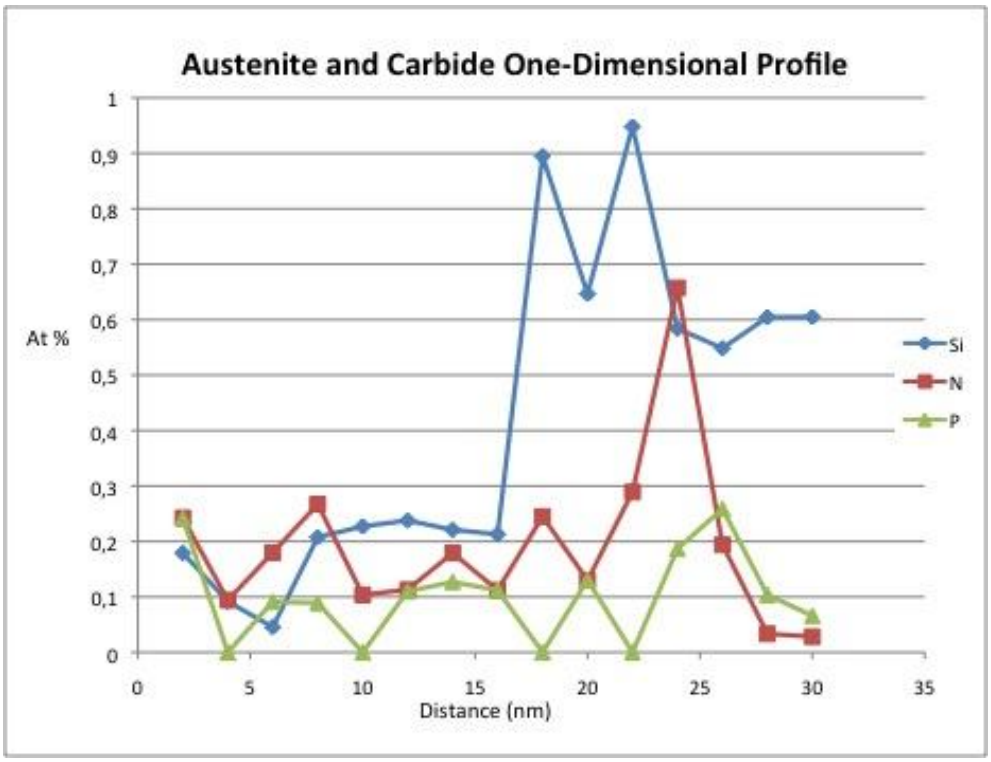

Figure 25: Low concentration of ions of Si, N and P present at the interface.

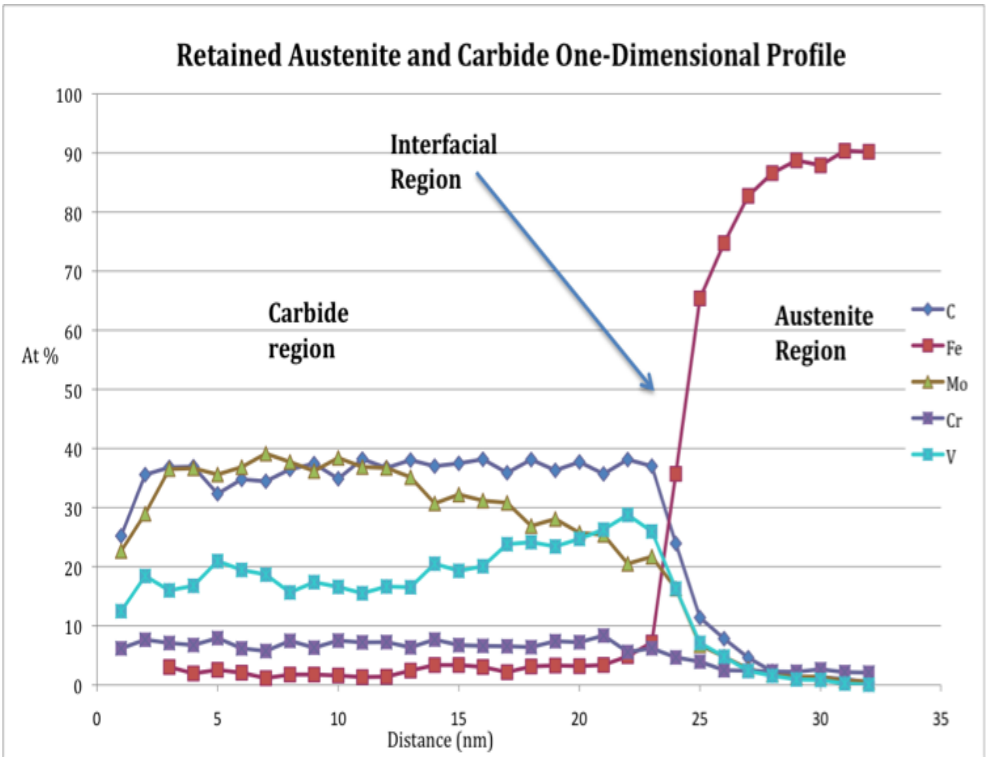

Figure 26: One-dimensional concentration profiles across an austenite-carbide interface.

- **Retained austenite-martensite interface:**

Fig.27 shows concentration profiles across the interface between the retained austenite and the martensite. It shows that the austenite has a higher concentration of Mn, almost 4.5 at.%. There is a small increase in Cr in the austenite region.

Fig.27 also shows traces of high concentration of silicon near the interface. It lies nearly outside the interface, towards the austenite region. Silicon works as stabilizer and deoxidizer. It provides stability to carbides, which in turn gives a good strength to steel [10]. In QRO type materials, high amount of silicon is found near the interfaces.

Fig.28 shows traces of P, B and N at the interface. Nitrogen is randomly distributed around the interface. At some analyses it has some higher concentration near the interface but it is hard to say that it lays at the interface boundary. No pictorial evidence of nitrogen at the interface has been found.

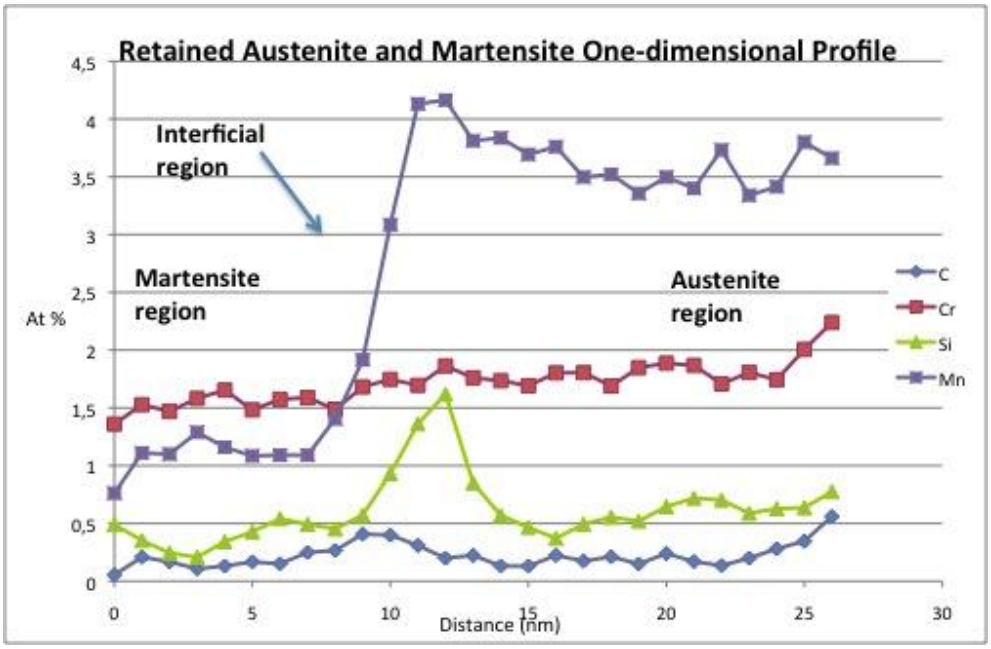

Figure 27: One dimensional concentration profile showing different regions of interest.

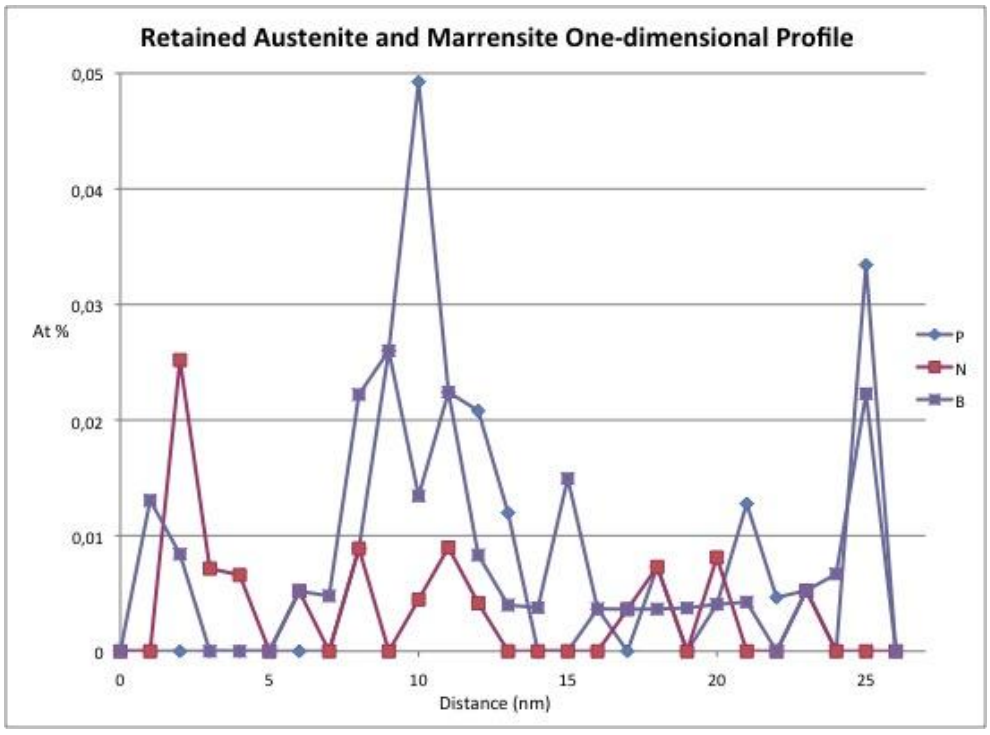

Figure 28: Traces of few ions of P, B and N present at the interface between retained austenite and martensite region.

3.3 QRO 90 (ART)

3.3.1 Tomographic reconstruction:

The atom probe measurements were performed at laser pulsing mode with a laser energy of 0.3 nJ, frequency of 200 kHz and the specimen temperature of 54 K. A few million counts were recorded. Fig.29 shows the tomographic reconstruction of the QRO 90 ART. Table 15 presents the bulk composition of the material.

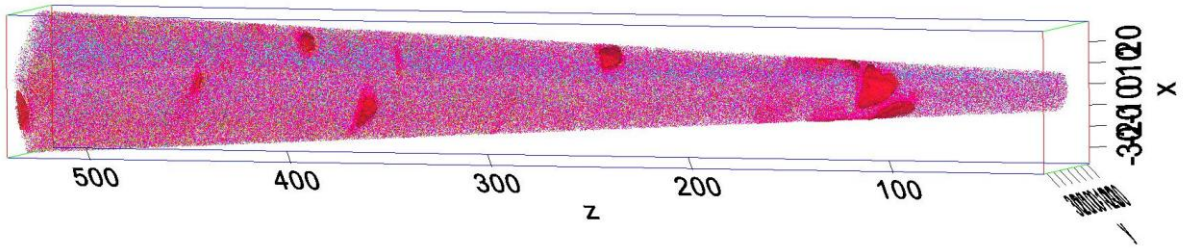

Figure 29: Tomographic reconstruction of QRO 90 (ART). The red precipitates are carbides highlighted by iso-concentration surfaces of C, Mo and V while the pink dots are mainly Fe ions.

Table 15 Composition of bulk (at.%)

Elements	*Ions*	*At %*
Fe	25939796	94.3
Cr	498571	1.8
Si	230372	0.8
Mn	203030	0.7
Mo	112833	0.4
V	104889	0.4
C	89009	0.3
N	3009	0.01
Ni	71619	0.3
Cu	24759	0.1
Total Ions	27507554	

3.3.2 Carbides:

After tempering, the carbides in QRO 90 ART have a radius in the range 0.8-5 nm. The carbides seem to contain more vanadium and becoming V-rich instead of Mo-rich. Mo and V are homogenously distributed inside the carbides. Fig.30 shows the tomographic

construction of carbides found in QR0 90 ART. Measuring the carbon concentration, it is considered that most of the carbides are MC-type with high solubility for V and Mo. Few atoms of N have also been observed in QRO 90 ART but they are considered to be as impurities. Table 16 shows the concentration of carbides and their approximate equivalent radius. Table 17 presents the details about the ions found in the matrix excluding the carbides.

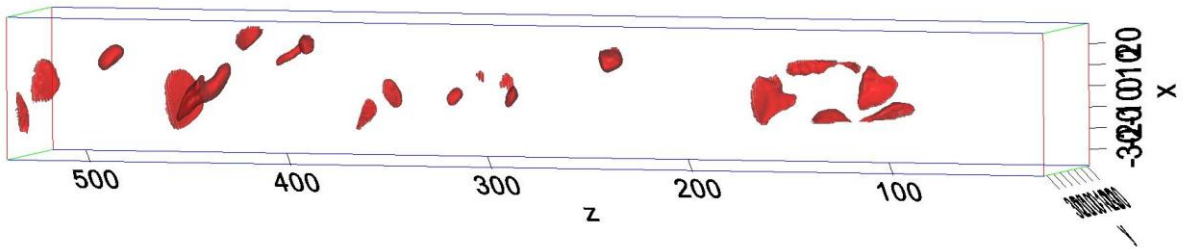

Figure 30: Iso-concentration surface of Mo, V and C (55x60x510 nm).

Table 16 Composition of elements found in QRO 90 ART and their approximate equivalent radius.

Run 2648	*C*	*V*	*Mo*	*Cr*	*N*	*Fe*	*Total Ions*	*Radius (nm)*
MC	35.3	25.9	18.5	7.3	0.7	4.3	20253	4.9
MC	38.6	25.6	20.5	7.6	0.5	3.7	9323	3.8
MC	40.7	26.8	18.4	7.6	0.8	0.6	8050	3.6
MC	34.5	31.8	20.7	6.1	0.3	3.4	7724	3.5
MC	31.5	27.1	20.5	8.5	0.4	5.8	6304	3.3
MC	34.2	25.7	23.9	6.2	0.4	5.4	5548	3.2
MC	36.5	32.1	20.3	6.0	0.8	1.6	5386	3.1
MC	39.1	37.4	13.3	5.5	0.5	1.0	3098	2.6
MC	35.4	27.1	16.0	7.3	0.3	5.8	2756	2.5
MC	27.3	26.7	18.3	7.8	1.0	12.2	2513	2.4
MC	34.7	29.3	16.9	5.6	0.8	7.1	2465	2.4
MC	42.5	25.1	18.1	6.3	0.8	0.5	2411	2.4
MC	36.7	28.9	20.1	6.9	0.8	1.6	1892	2.2
MC	40.2	30.2	15.7	6.6	0.5	1.0	1140	1.9
MC	39.0	28.0	16.2	5.4	0.6	2.0	753	1.6
MC	39.6	29.7	18.4	5.6	1.7	1.0	264	1.1
MC	45.6	24.0	17.6	5.7	1.5	-	79	0.8

Table 17 Composition of matrix (at.%).

Elements	*Counts*	*At %*
Fe	24527205	95.1
Cr	453298	1.8
Si	214589	0.8
Mn	189510	0.7
Mo	65364	0.3
Ni	62814	0.2
V	31749	0.1
Cu	22355	0.1
Total Ions	25789356	

3.3.3 Martensite-carbide interface:

Fig.31 shows the concentration of elements making up the carbides. It is seen that the carbides have high enrichment of V at the interface and it decreases towards the center of the carbide. It can be concluded that the growth of the carbide is dependent on the mobility of V inside the matrix. The carbide also has some solubility for Cr and Mn.

The alloying element like Si, Ni, P, Cu and few ions of nitrogen are also present at the interface as shown in the fig.32. The alloying element has also significant role to play in the growth of the carbide and on the tempering resistance.

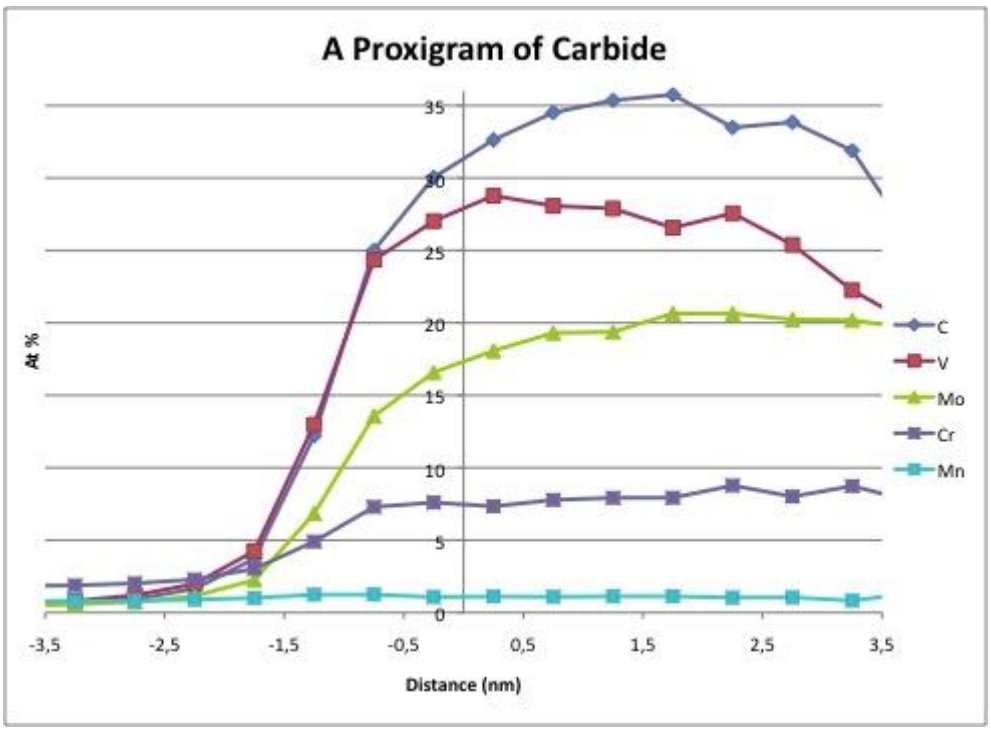

Figure 31: A proxigram of carbides showing concentrations of C, V, Mo, Cr and Mn.

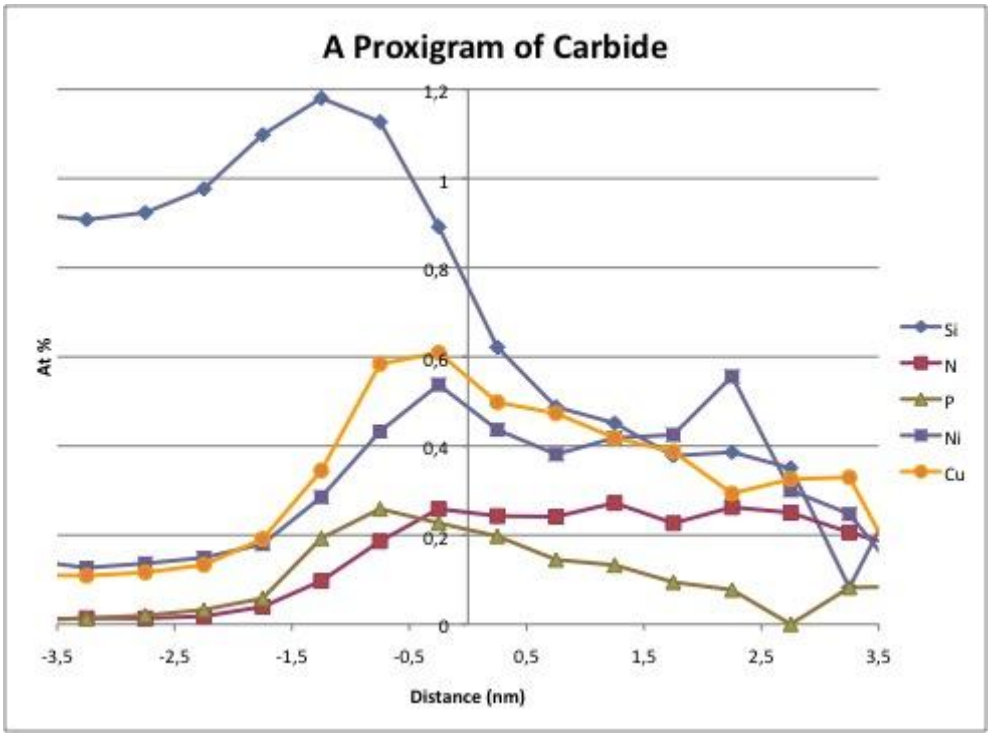

Figure 32: A proxigram of carbide with low concentration of alloying elements.

3.4 QRO 80N (ART)

3.4.1 Tomographic reconstruction:

Several samples were investigated through the atom probe. The measurements were performed at laser pulsing mode with a laser energy of 0.3 nJ, frequency of 200 kHz and the specimen temperature of 54 K for Run 2651, 72 K for Run 2715 and 63 K for Run 2717. A Few million counts were recorded. Fig.33, fig.34 and fig.35 show the tomographic reconstruction of QRO 80N ART. Table 18 present the bulk concentration of the material.

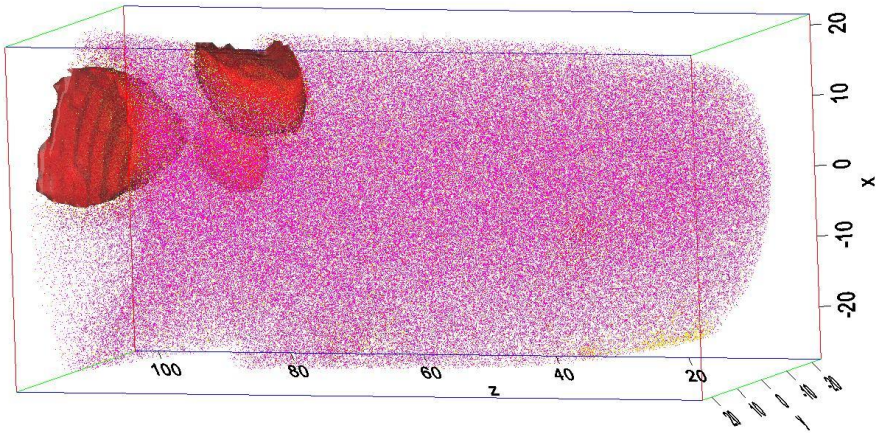

Figure 33: Tomographic image from run 2715. The red precipitates are carbides (highlighted by iso-surfaces) (45x40x100 nm).

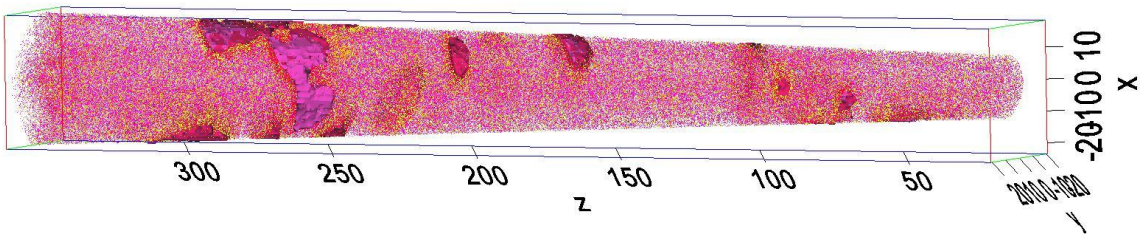

Figure 34: Tomographic image from run 2717. The small pink color precipitate is a Mo-rich carbide while red precipitates are carbides (highlighted by iso-surfaces) (30x40x350 nm).

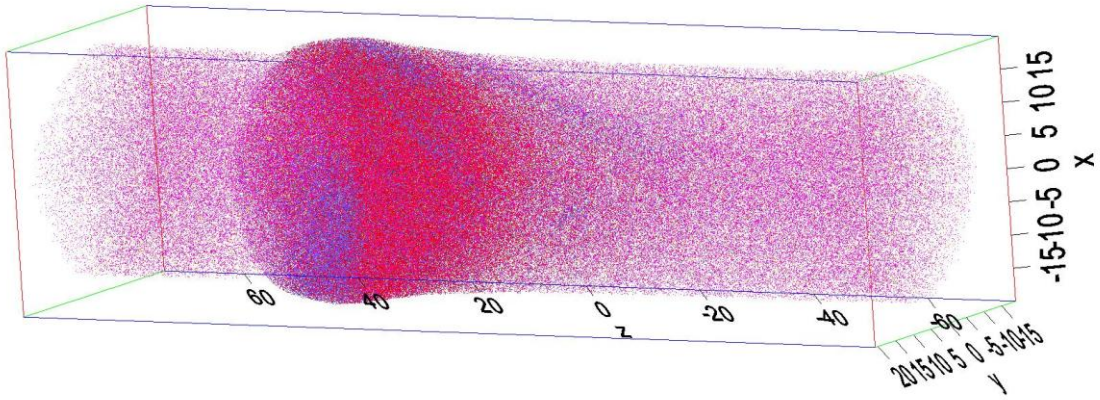

Figure 35: Tomographic image from run 2651 (35x30x 190 nm). Blue dots are V atoms and red dots are Mo.

Table 18 Composition of bulk (at.%).

Elements	*Ions*	*At %*
Fe	7979775	91.4
Cr	144686	1.7
C	139547	1.6
Mo	130729	1.5
V	117651	1.3
Mn	94427	1.1
Si	69399	0.8
N	21297	0.001
Ni	11066	0.1
Total ions	8726635	

3.4.2 Carbides:

Fig 36, fig.37 and fig.38 show the iso-surfaces of C, Mo and V found in run 2715, run 2717 and run 2651, respectively. Evaluating the results, it seems like the coarsening of the secondary precipitates of QRO 80N ART has disturbed the homogenous distribution of Mo and V inside the carbides. Table 19 shows the composition of carbides found in QRO 80N ART.

- The carbides have grown with tempering and the precipitates have radii of around 2-6 nm (if they are assumed to be spherical).
- The carbide composition is changing towards being more V-rich instead of being Mo-rich (compared to 1 hr tempered).
- There are traces of high and low concentration regions of Mo and V inside the carbide as shown in fig.39. Some precipitates with high enrichment of Mo have also been found, shown in fig.37. The details of the Mo-rich precipitate are presented in table 20.
- Nitrogen has high affinity for vanadium as shown in the fig.40 (also compare with table 19).
- All the N and V seem to be consumed by the carbides (compare table 18 and table 21).

From the above points, it can be deduced that there is high mobility of V inside the matrix causing the carbide to form high and low concentration regions of Mo and V. In the V-rich parts of carbides, high concentrations of nitrogen have been found as shown in fig.40. It can be seen that N has high affinity for vanadium rich carbides. This somehow shows the impact of nitrogen during coarsening. Table 21 shows that there are some ions of N and V in the matrix; this suggests that the process of redistribution of V and N will still continue with more tempering hours.

The carbon concentration inside the carbides is around 35-40% due to the inefficiency of detector to measure carbon correctly. The carbides are considered to be MC type except for the carbide presented in table 20, found in run 2717. It is thought that the carbide is in its transformation phase.

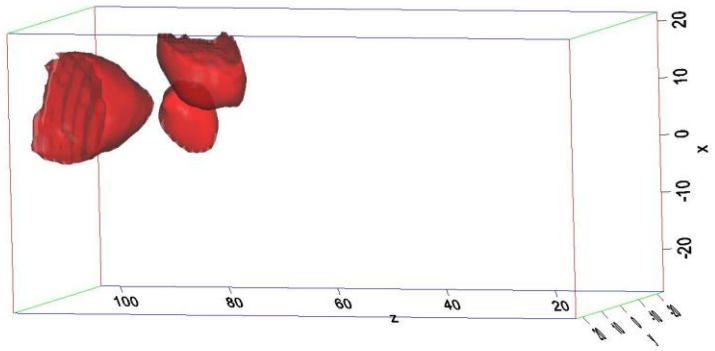

Figure 36: (Run2715) Iso-concentration surface of Mo, V and C (45x40x100 nm).

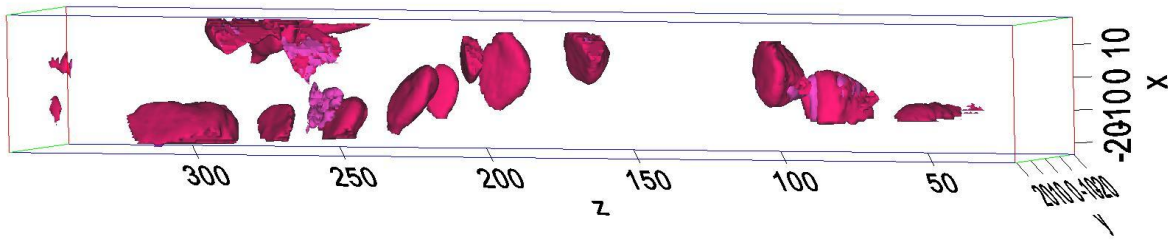

Figure 37: Iso-concentration surface of Mo, V and C. The pink precipitate is Mo-rich from Run 2717 (30x40x350 nm).

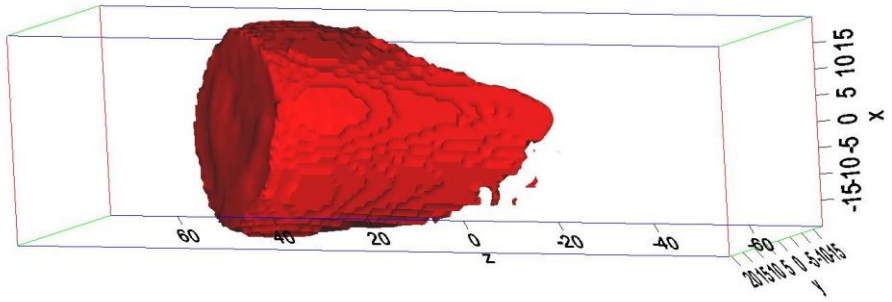

Figure 38: Iso-concentration surface of Mo, V and C from Run 2651 (35x30x 90 nm).

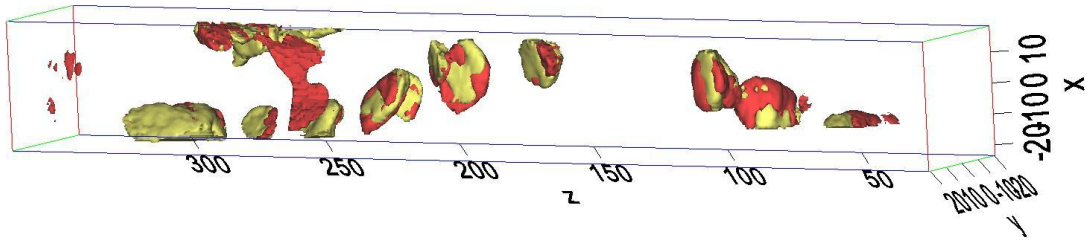

Figure 39: Tomographic image of V (yellow color) and Mo (red color) showing their inhomogeneous distribution inside the carbide (30x40x350 nm).

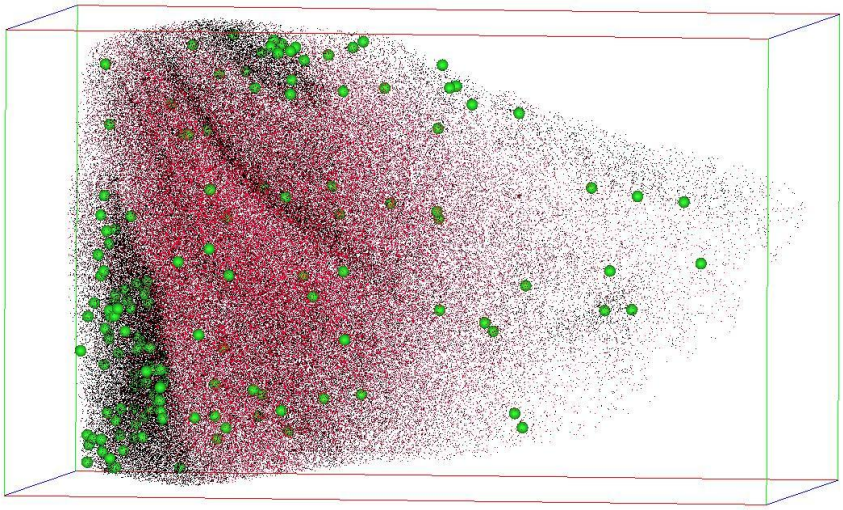

Figure 40: Presence of N in V-rich region of the carbides. Also, it shows Inhomogeneous distribution of Mo and V inside the carbide. (The red dots are Mo ions, black dots are V ions and green dots are N ions, 35x30x 90 nm).

Table 19 Composition of carbides (at.%) and approximate equivalent radius.

Run 2715	*C*	*Mo*	*V*	*Cr*	*Fe*	*N*	*Total counts*	*Radius (nm)*
MC	37.4	26.9	24.8	5.5	4.37	1.06	16010	4.5
MC	35.7	29.8	25.5	5.3	2.76	0.94	15933	4.5
MC	38.4	22.9	29.1	4.9	3.75	0.92	4484	2.9
Run 2717								
MC	37.4	21.2	32.7	5.2	2.5	1.1	35290	5.9
MC	39.3	21.1	31.6	4.8	2.4	0.8	23462	5.1
MC	35.9	19.2	37.6	3.9	2.2	1.1	10043	3.9
MC	39.9	22.3	30.5	4.3	2.0	1.1	9146	3.7
MC	35.3	21.8	31.5	5.9	4.5	1.1	8066	3.6
MC	35.7	28.3	26.1	4.9	4.2	0.7	4788	3.0
MC	41.1	14.4	37.1	3.7	2,7	1.1	4488	2.9
MC	37.1	36.0	17.1	6.6	2.5	0.7	3435	2.7
MC	40.0	16.0	37.0	4.0	2,2	0.8	2956	2.6
MC	36.1	18.3	37.3	4.2	2.8	1.3	2772	2.5
MC	39.1	19.5	34.0	3.4	2.4	1.4	2027	2.3
MC	37.5	21.7	31.1	4.8	3.8	1.2	1449	2.0
Run 2651								
Big Carbide	34.8	40.8	11.1	9.9	2.8	0.6	981442	17.8
V-rich of big carbide	39.0	15.0	35.6	5.7	3.3	1.4	67020	7.3

Table 20 Composition of Mo-rich precipitate found in run 2717.

Element	*C*	*Mo*	*V*	*Cr*	*Fe*	*Si*	*Mn*	*N*	*Counts*	*Radius (nm)*
Mo-rich	13.5	38.7	1.4	4.8	32.3	7.3	1.8	0.18	5293	3.1

Table 21 Composition of matrix (at.%)

Elements	*Ions*	*At %*
Fe	3404587	94.0
Cr	57648	1.6
Mn	48628	1.3
Si	19865	0.5
Mo	9669	0.3
Ni	46514	1.3
C	2282	0.06
V	3492	0.1
N	824	0.02
Total ions	3618543	

3.4.3 Martensite-carbide interface:

It seems that some carbides dissolve during tempering providing new V for small carbides. The vanadium content in the carbides increases drastically with few hours of tempering. Fig.42 shows the decreased concentration of Mo and increasing concentration of vanadium inside the carbides. It also suggests that the carbides have a V-rich core. Comparing fig.42 and fig.43, the at.% of V and N increases inside the core of the carbides. It can be seen that the vanadium and nitrogen curves follow the same increasing pattern showing the high affinity of nitrogen for vanadium. This could also be seen in the tomographic reconstruction. The cross-section in fig. 41 (left) shows the presence of P and B at the interface while (right) shows the enrichment of nitrogen inside the carbide.

Small enrichments of P, Ni, B, Si and N at the interface are shown in fig.43. The low concentration-alloying element has a significant role in secondary precipitation.

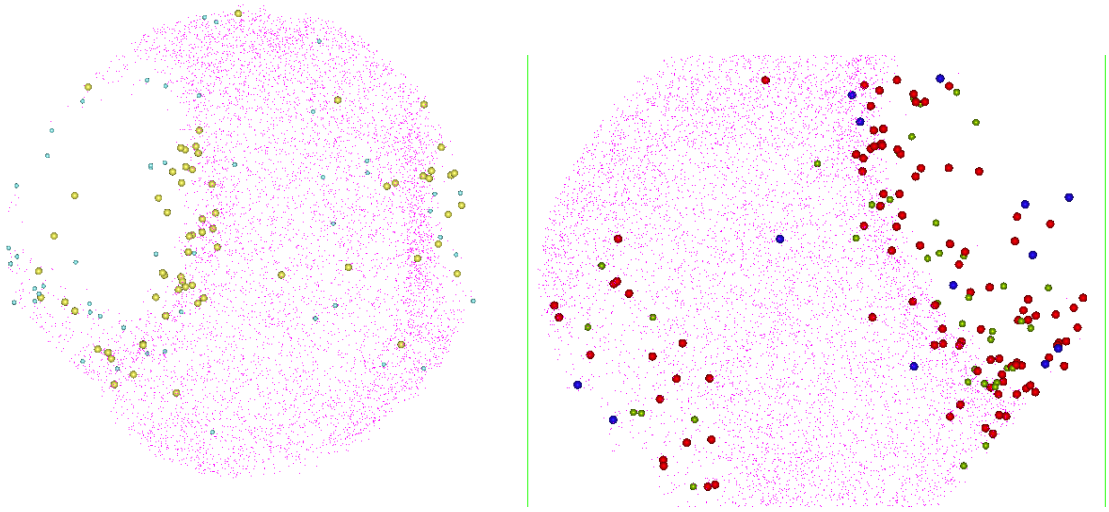

Figure 41: The cross sectional picture (left) shows the presence of P (yellow) and B (blue) ions at the interface between carbide and matrix (pink). The cross-sectional picture (right) shows the N (green), MoN (red) and VN (blue) ions inside the carbide (empty region) and at the interface between carbide and matrix (pink).

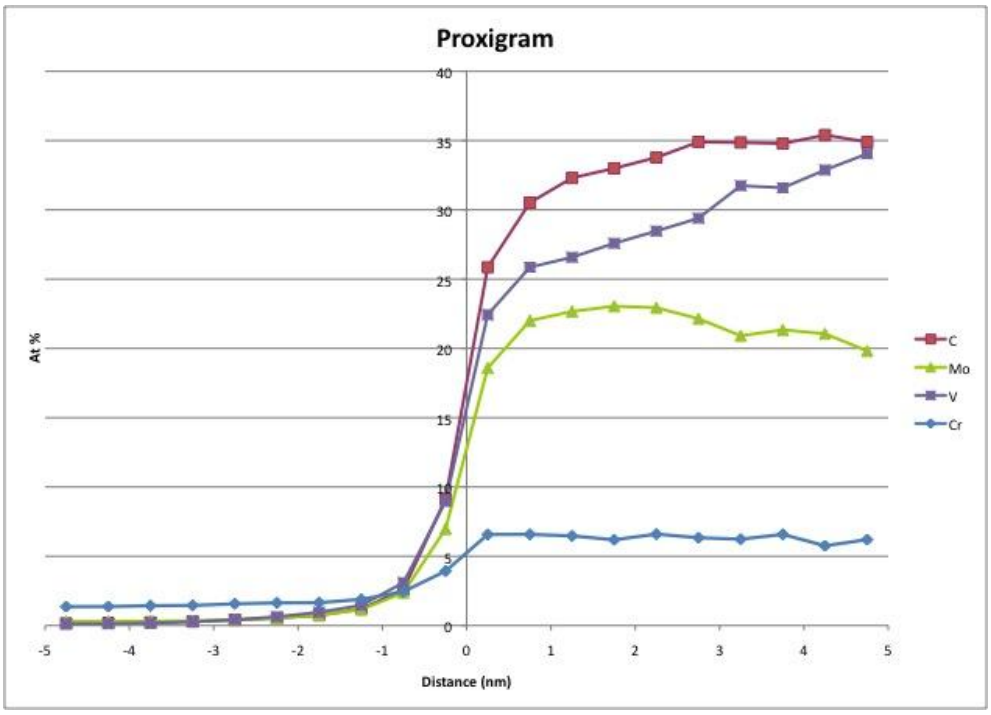

Figure 42: A proxigram showing the increasing V concentration inside the carbide. Positive *x*-axis is the carbide while negative *x*-axis is the matrix.

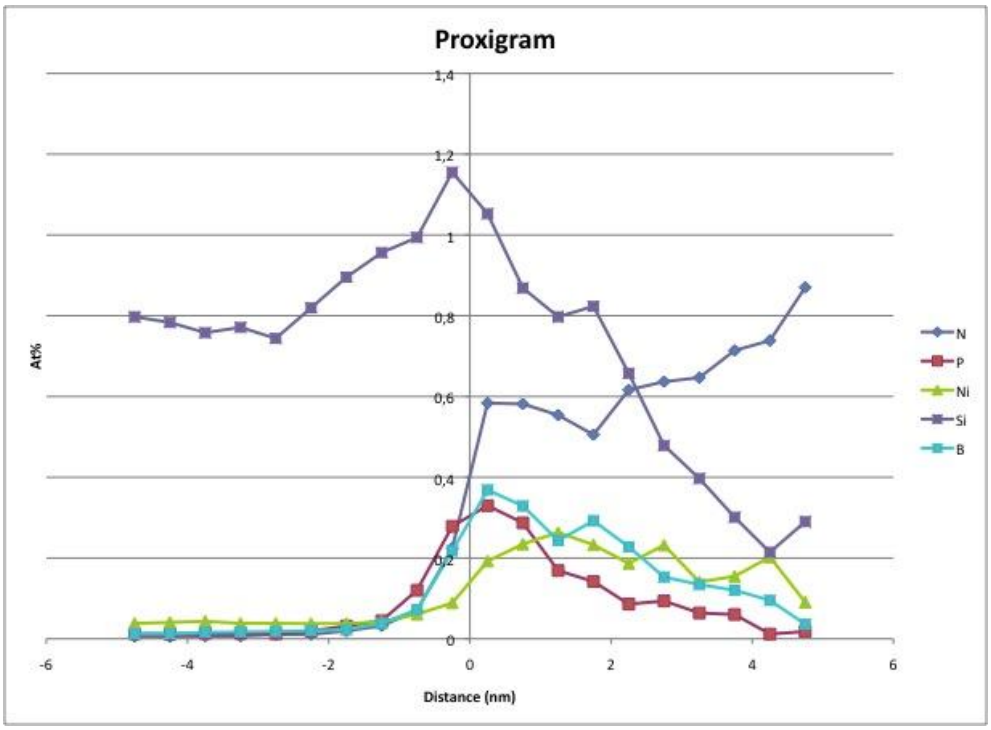

Figure 43: A proxigram showing the presence of alloying elements at the interface. The increasing N content behaves the same way as V inside the carbide.

4. Experimental Difficulties

During evaluation of the data, unique behaviors of silicon ions were observed in the tomographic reconstruction. They seem to be distributed along certain lines, forming regions of high and low density along the *z*-axis. This is a common artifact in atom probe analysis especially for silicon in steels. It is shown in fig.44.

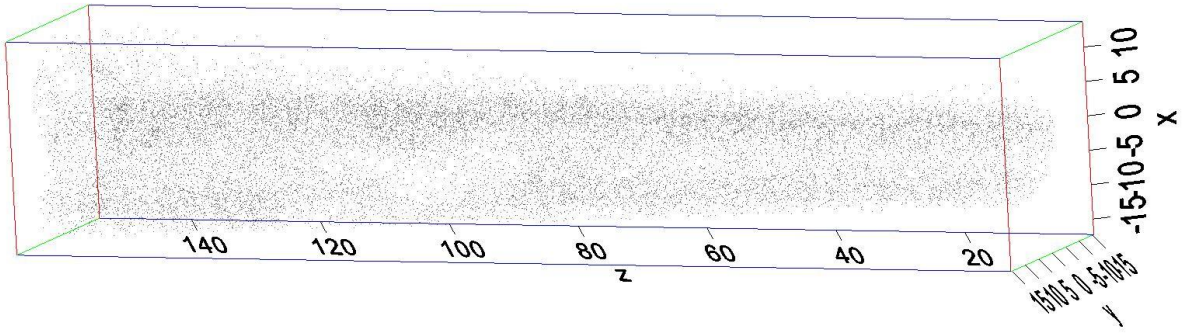

Figure 44: An artifact of silicon: The tomographic reconstruction shows an uneven distribution of silicon ions.

Usually silicon is more or less homogenously distributed in the iron matrix except for different interfaces. Silicon enrichment is very obvious at the carbides interfaces in the analyses of the QRO materials. Fig.45 (right) shows the two-dimensional density of silicon imaged along the *z*-axis. The red regions show high density of ions while the density decreases with yellow, green and blue, respectively. Fig.45 (left) shows a two-dimensional cross sectional view of the whole reconstruction. The red line is the *x*-axis while the green line is the *y*-axis.

The artifact is due to the migration of silicon atoms on the surface of the tip. It was also observed for P. If the local field is not high enough to liberate the ions from the tip surface, it provokes the ions to be surface migrated. The ions move to different field zones on the surface until they are field evaporated. Surface migration occurs due to the following reasons:

- Surface migration is dependent on the radius of the ions. Small atoms can find more stable regions over the surface [12].
- R(N) < R(C) < R(P) < R(Si) < R(Fe) < R(Mn) < R(Nb)

- It is dependent on the temperature of the tip and is directly proportional to the laser power [12].

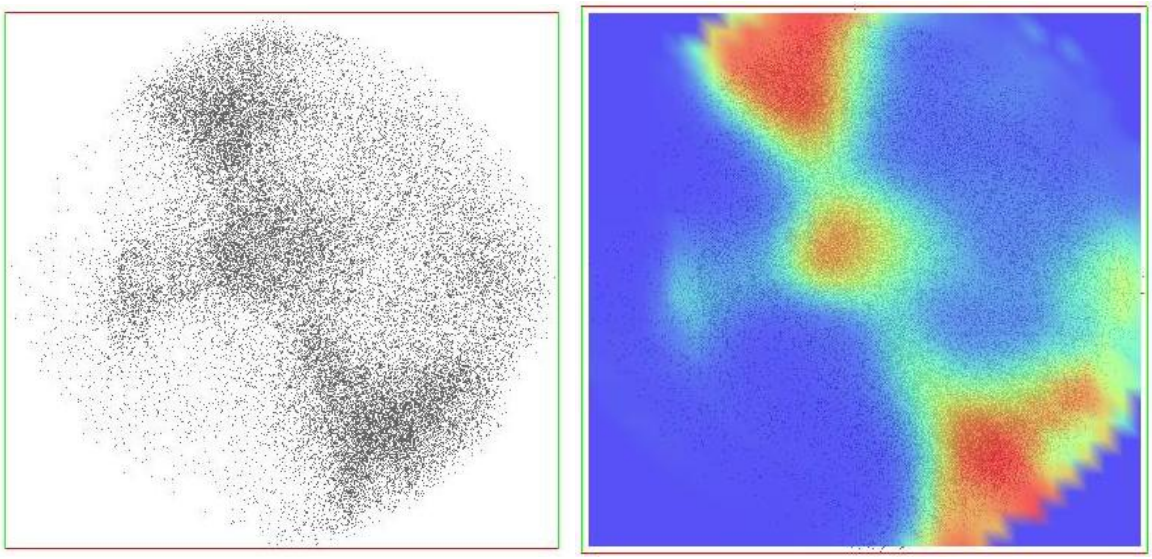

Figure 45: Crossectional images perpendicular to the *z*-axis (left); formation of poles of silicon ions on the reconstructional image. The crossectional density of Si ions along *z*-axis (right), the density of Si ions decreases with red, yellow, green and blue respectively.

5. Short Discussion

Comparing the hardness curves for the material QRO 80 N and QRO 90, QRO 90 is austenized at high temperature giving it higher initial hardness. It was observed that not always a high initial hardness provides a good tempering resistance [5]. QRO 80 N has a somewhat lower initial hardness but it has a better tempering resistance. During the first 30 hours of tempering there is a quick decline in the hardness whereas good tempering resistance is achieved in later hours of tempering. Tempering resistance stability is reached around 100 hours to 1000 hours.

It is seen that during the first 30 hours of tempering, there is a morphological difference between the precipitates of QRO 80 N and QRO 90. However, both materials have the same kind of carbides with a mix composition Mo-V-Cr. The precipitate can be divided in two types considering their shape to be spherical. There are big carbides (few) with radius > 2 nm and small precipitates (many) with radius < 2 nm. With carbon measurements these carbides are considered to be MC-type with a high concentration of Mo and V. The number density of carbides in the materials is shown in the table 23. It explains that the small carbides are dissolving to form bigger carbides thus reducing the number density.

Table 23 Number density of carbides before and after annealing resistance tempering.

Material	*Density of carbide (carbides/nm^3)*
QRO 80 N	5.8×10^{-5}
QRO 90	5.3×10^{-5}
QRO 80 ART	1.7×10^{-5}
QRO 90 ART	1.1×10^{-5}

Initially the carbides are Mo-rich but after tempering for 30 hours the carbides become V-rich. This behaviour during thermodynamical growth of secondary precipitates is the same for both materials. Fig.46 shows the average concentration change in Mo and V within the precipitates in both materials. The only difference in the carbides is that QRO 80 N has high and low concentration regions of Mo and V, in contrast QRO 90 has a homogenous distribution of Mo and V. Also in QRO 80N, the Mo rich part of the carbide has high Cr in its core whereas in V-rich parts it seems to be completely opposite. The presence of Cr inside the carbide might produce Cr enriched carbon precipitation in the later phase of tempering.

The difference in the morphology of the secondary precipitate can be a result of the nitrogen addition in the material QRO 80 N. There are signs of high amounts of nitrogen ions in the vanadium rich areas of the secondary precipitates showing the high affinity of N for V.

Followed by the previous work on the same material it was considered that the secondary precipitate goes through an evolutionary phase. During the secondary stage of precipitation phase, M_2C (Mo-V-Cr) will dissolve and V will take part in further precipitation of MC carbide, Mo will take part in further growth of M_6C and Cr with C will form precipitates of equilibrium carbide $M_{23}C_6$. [5]

Equilibrium phase carbide has not been observed through atom probe investigations. Since QRO 80 N and QRO 90 belong to the same family of steels, it is believed that a similar kind of phase transformation of MC carbides (i.e the distribution of Mo and V in to region of high and low concentration) will also occur in QRO 90 but at some later stage of tempering. This early phase transformation of MC carbides in QRO 80N can also be a consequence of nitrogen addition and might be one of the reasons behind QRO 80N's good tempering resistance.

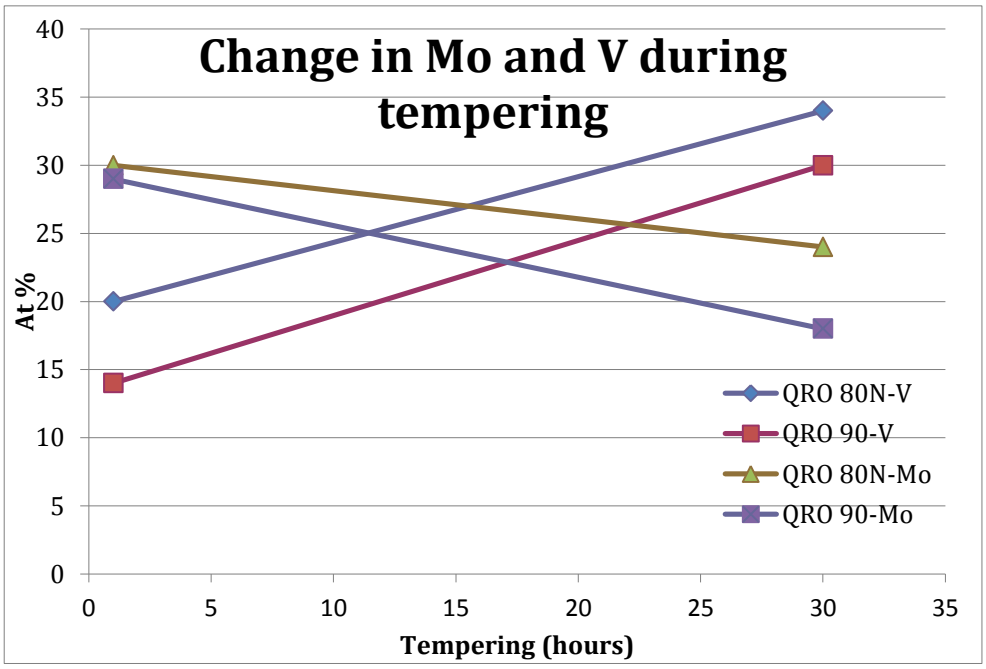

Figure 46: Average concentration of Mo and V in MC during tempering.

6. Conclusions

- QRO 80N and QRO 90 contain the same type of carbides. They are considered to be MC-type. These carbides have a mixed composition of Mo and V with low amounts of Cr and Mn. The fresh material contains Mo-rich carbides. After tempering of 30 hours the carbides become V-rich.

- Due to tempering, small precipitates dissolve and bigger precipitates are formed thus reducing the number density of carbides with tempering (coarsening).

- After tempering for 30 h, QRO 80N has an inhomogeneous distribution of Mo and V inside the carbides. In contrast QRO 90 has homogenous distribution of Mo and V inside the carbides. It can be concluded that nitrogen additions cause an early phase transformation of carbides in QRO 80N or this could be due to the difference of chemical composition of the materials as QRO 80N has significantly higher amounts of Mo, V, Mn and a lower amount of Cr as compared to QRO 90.

- N forms molecular ions (like MoN and VN) in the atom probe analysis of the materials. Few atoms of N (peak at 7 Da) were observed. This makes it very hard to detect nitrogen atoms with good accuracy.

- N has high affinity for V and most of it is found at the interface or inside the V-rich precipitates.

7. Acknowledgements

I would like to thank all the people who put positive energy in this work. I am sure that it would not be possible without the help and support of the following people. I respect and admire them:

- My supervisor, Dr. Mattias Thunvander for his long hour discussions and his ability and humbleness towards answering all type of questions that I have asked him. I am greatly thankful to him for helping me from the lab preparation to thesis writing.
- My brother, Mr. Omar Khan for all his support and his attitude towards life. Also for inviting me to live in Gothenburg. I have learned a lot from him.
- Prof. Hans-Olof Andren for his discussions, and to all the wonderful people in the group of Microscopy and Microanalysis (Chalmers University) for their healthy conversations during the coffee break.
- Mr. Ola Löfgren and Dr. Anders Kvist for their technical support during the work.
- Dr. Jörgen Andersson for inviting me to Uddeholm to present this thesis work.
- This study work was supported by Uddeholm AB. I am thankful to them for providing me with such opportunity.
- To all my friends and family members.

Let the beauty of what you love,

Be what you do.

Rumi

8. References:

[1] Jörgen Andersson, Secondary hardening in some low-chromium hot-work tool steels, Department of applied physic, Chalmers university of Technology, 2011.

[2] Jörgen Andersson, Hans-Olof. A, Lars-Erik .S, Microstructural evolution during quenching and tempering in hot-work tool steels UDDEHOLM QRO 90 Supreme, Dept. of applied physics, Chalmers University of Technology, 2011.

[3] Nordström L-Å. Development of a martensite hot-work tool steel. Internal report, Uddeholm tooling AB, 1972.

[4] Gavriljuk.V.G, Shanina.B.D, Berns.H, A physical concept for alloying steels with carbon + nitrogen, Material Sci. and Eng. A, vol 481-482, 707-12, May 2008.

[5] Jörgen Andersson, Mattias Thuvander, Hans-Olof. A, Lars-Erik .S, Tempering resistance of some hot-work tool steels, Dept. of applied physics, Chalmers University of Technology, 2011.

[6] Nordström L-Å, Hardening mechanism in Tool Steel, internal report, Research and Development, Uddeholm tooling AB, 2003.

[7] P.P. Camus and A.J.Melmed, Surf.Sci. 246, 415,1991.

[8] M.Thuvander, J. Weidow, J. Angseryd, L.K.L Falk, F.Liu, M. Sonestedt, K.Stiller, H.-O.Andren, Quantitative atom probe analysis of carbides, Ultramicrosopy 111, 604-608, 2011.

[9] Thomas F.Kelly, Michael.K.Miller, Atom Probe Tomography, Review of Sc.Inst. 78, 2007.

[10] R. Honeycombe,H.K. Bhadeshia, Steels Microstructure and Properties, 2nd Edittion, 2003.

[11] Jörgen Andersson, Hans-Olof.A, Lars-Erik.S, Nitrogen in low chromium hot-work tool steel: a modeling and experimental study, Dept. of applied physics, Chalmers University of Technology, 2011.

[12] B.Gault, F. Danoix, K. Hoummada, D. Mangelinck, d. Leitner, Impact of directional walk on atom probe microanalysis, Ultramicroscopy, 2011